Numerical Studies of Jet-Wing Distributed Propulsion and a Simplified Trailing Edge Noise Metric Method

Jessica Nicole Walker

A Thesis submitted to the Faculty of
Virginia Polytechnic Institute and State University
In partial fulfillment of the requirements for the degree of

Master of Science
In
Aerospace Engineering

J.A. Schetz, Chair
W.H. Mason
B. Grossman

August 25, 2004
Blacksburg, Virginia

Keywords: Computational Fluid Dynamics, Jet-Wing, Jet-Flap,
Distributed Propulsion, Trailing Edge Noise

Numerical Studies of Jet-Wing Distributed Propulsion and a Simplified Trailing Edge Noise Metric Method

Jessica N. Walker

(ABSTRACT)

In recent years, the aircraft industry has begun to focus its research capabilities on reducing emissions and noise produced by aircraft. Modern aircraft use two to four engines arranged on the wing or behind to produce thrust that is concentrated directly behind the engine. Kuchemann suggested a way to improve the propulsive efficiency by changing the normal configuration of engine and aircraft. This concept is the jet-wing distributed propulsion idea, which redistributes the thrust across the span of the wings. Distributed propulsion is accomplished by using many smaller engines spread across the wings or several large engines to duct the exhaust flow in a jet-wing. The jet-wing concept can be used to reduce noise and also as a replacement for flaps and slats by deflecting the jet. Since the distributed propulsion concept is also a method to reduce noise, it's important to have a simplified method of calculating the trailing edge noise of a wing.

One of the purposes of this paper was to study the effect of adding jet-wing distributed propulsion to a thick "inboard" airfoil. The two-dimensional jet-wing model was analyzed by parametric computational fluid dynamic (CFD) studies using the Reynolds-averaged, finite-volume, Navier-Stokes code GASP. The model was set up to be self-propelled by applying velocity and density boundary conditions to the blunt edge of the airfoil. A thick "inboard" airfoil from a realistic transonic wing was needed for the study, and the $\eta = 0.226$ span station of the EET Wing was chosen. This airfoil was thick with a thickness

to chord ratio of 16%. In adding distributed propulsion to this thick airfoil, it was found that there was an increase in the propulsive efficiency as compared to typical modern high-bypass-ratio turbofan engines with no negative aerodynamic consequences.

The other purpose of this study was to create and assess a simplified method to calculate the trailing edge noise metric value produced by an airfoil. Existing methods use RANS CFD, which is computationally expensive and so it seemed important to find a less expensive method. A method was formed using the Virginia Tech Boundary Layer Java Codes which calculated the characteristic turbulent velocity and characteristic turbulent length scale. A supercritical airfoil, SC(2)-0714, was used to assess the simplified method as compared to the more computationally expensive GASP runs. The results showed that this method has trends that follow those of the GASP results with the methods comparing well up to modest lift coefficients.

Acknowledgements

First, I would like to thank my parents, Bryan and Julie, for all of their love and support through out my college career. With out them none of this would be possible. They have been there for me and gave me a very strong foundation from which to build my life. I know they will all ways be there if I need them. I am also thankful to my brother and sister for all of their faith in my success. B.K., you are a wonderful brother and all of your encouragement hasn't gone unnoticed. And Brittany, your never failing faith in me has been a big help in all of my accomplishments. Another big help to me through this whole process have been my grandparents, Ralph and Mildred Sunderland. Their encouragement and support have been a great help to me. And to the rest of my family, who have all given me love and support throughout my life, I thank them sincerely. I love you all!

I would also like to thank my advisor, Dr. Schetz for all of his guidance and support. He helped me to join the Blended-Wing Body design group and to begin my work with computational fluid dynamics. All of his suggestions and insights have invaluable to the work I've done with distributed propulsion and trailing edge noise.

The other members of my committee also deserve some recognition. Dr. Mason's and Dr. Grossman's time and support thorough out this process have been truly helpful. I want to thank them for all of the help they have given me. I also acknowledge the other members of the Blended-Wing Body Design group, especially Serhat Hosder and my predecessor, Vance Dippold, for all of their assistance through out this project. I am also thankful to Dr. Haftka for the help he gave. I am very proud to have worked with all of you.

Lastly, I wish to thank the support of the people at NASA Langley. This project would not have been possible without their financial support.

Table of Contents

List of Figures

List of Tables

Nomenclature

BL	Boundary Layer
BWB	Blended-Wing-Body
CFD	Computational Fluid Dynamics
MDO	Multidisciplinary Optimization
NASA	National Aeronautics and Space Administration
NACA	National Advisory Council for Aeronautics
NM	Noise Metric
TE	Trailing Edge
TKE	Turbulent Kinetic Energy

a	Speed of sound
a_∞	Freestream speed of sound
a_{jet}	Jet flow speed of sound
b	Wing span
b_{jet}	Span of jet-wing
c	Chord length
c_{2D}	Chord length for two-dimensional analysis
C_D	Drag coefficient
$C_{D_{net}}$	Net drag coefficient, includes jet thrust
$C_{D_{local}}$	Local drag coefficient, with respect to span
C_{Dw}	Empirical boundary layer constant = 0.09
C_f	Skin Friction Coefficient
C_J	Jet thrust coefficient
C_L	Lift coefficient
$C_{L_{net}}$	Net lift coefficient, includes jet thrust
$C_{L_{2D}}$	Lift coefficient for two-dimensional analysis
C_p	Pressure coefficient

D	Drag
D_{local}	Local drag, with respect to span
D_{Net}	Net drag, includes jet thrust
$\vec{F}$	Generic force vector; specify using pressure, viscous, momentum flux
Fx_Inv	Inviscid force in x-direction
Fx_Total	Total force in x-direction, not including momentum flux forces
Fx_Vis	Viscous force in x-direction
Fy_Inv	Inviscid force in y-direction
Fy_Total	Total force in y-direction, not including momentum flux forces
Fy_Vis	Viscous force in y-direction
H	Distance to the ground (receiver)
h_{jet}	Jet height
I_{NM}	Noise intensity indicator
$\hat{i}$, $\hat{j}$	Unit vectors in x- and y-directions
L	Lift
L_{Net}	Net lift, includes jet thrust
l_t	Characteristic turbulent length scale
m	Jet flow mass
M	Local flow Mach number
M_∞	Freestream Mach number
M_{jet}	Jet flow Mach number
M_{2D}	Mach number for two-dimensional analysis
Mz_Inv	Moment about quarter chord from inviscid forces
Mz_Thrust	Total moment about quarter chord, includes momentum flux forces
Mz_Total	Moment about quarter chord from inviscid and viscous forces
Mz_Vis	Moment about quarter chord from viscous forces
p	Pressure
p_∞	Freestream pressure

p_{jet}	Jet flow pressure
$p_{TE_{upper}}$	Pressure at upper surface trailing edge
$p_{TE_{lower}}$	Pressure at lower surface trailing edge
Q	The set of variables defined in GASP used to specify the flow conditions: temperature, pressure, density, velocity, laminar and turbulent viscosities, and Mach number.
Q_∞	In GASP, the set of flow parameters specifying the freestream conditions.
Q_{local}	In GASP, the set of flow parameters specifying conditions at an individual cell.
q	Dynamic pressure
R	Gas constant
Re	Reynolds number
Re_c	Reynolds number based on chord length
Re_{trans}	Transition Reynolds number
S , S_{ref}	Jet reference area
$Surf$	Airfoil surface not including trailing edge
$\frac{t}{c}$	Thickness ratio
$\left(\frac{t}{c}\right)_{2D}$	Thickness ratio for two-dimensional analysis
T , $Thrust_{jet}$	Jet thrust
T_{jet}	Temperature of jet flow
T_∞	Temperature of freestream
T_0	Total, or stagnation, temperature
$Thrust_{GASP}$	Thrust force from GASP, not including jet inflow
$Thrust\_x$	Total force in x-direction, including momentum flux forces
$Thrust\_y$	Total force in y-direction, including momentum flux forces
u , v , w	Velocity magnitude in the x-, y-, and z-directions
u_{BL} , v_{BL}	Velocity magnitude in the x-, y-directions aligned with boundary layer
u_0	Characteristic velocity scale for turbulence

u_*	Friction velocity
U	Velocity magnitude
U_∞	Freestream velocity magnitude
U_{jet}	Jet velocity magnitude
U_e	Boundary layer edge velocity magnitude
$\hat{U}_x, \hat{U}_y, \hat{U}_z$	Component of velocity unit vector in x-, y-, and z-directions
x, y, z	Coordinates
y^+	Transverse coordinate for law of the wall
α	Airfoil angle of attack
β	Ratio of jet velocity to freestream velocity
β_{TE}	Trailing edge sweep angle
δ	Boundary layer thickness
δ^*	Displacement Thickness
δ_{ini}	Initial boundary layer thickness
δ_{TE}	Boundary layer thickness at trailing edge
γ	Ratio of specific heats
κ	Law of the wall constant = 0.41
η_P	Froude propulsive efficiency
η	Wing span station
$\Lambda_{1/4}$	Quarter-chord sweep
μ	Dynamic viscosity
μ_∞	Freestream dynamic viscosity
μ_{lam}	Laminar dynamic viscosity
μ_{vis}	Viscous dynamic viscosity
μ_T	Eddy Viscosity
$\mu_{T,O}$	Eddy Viscosity in the outer region of the boundary layer
$\mu_{T,\log}$	Eddy Viscosity in the log region of the boundary layer

θ	Momentum Thickness
ρ	Density
ρ_{∞}	Freestream density
ρ_{jet}	Jet flow density
τ	Jet deflection angle
τ_{w}	Wall shear stress
ν	Kinematic viscosity
ω_{0}	Characteristic source frequency

Chapter 1: Introduction

Aviation plays a large part in today's society and companies are always seeking bigger and better ways to improve the aircraft industry. Two of the largest efforts are involved with improving aircraft noise and emissions [2].

The concept of distributed propulsion is one of the ideas that has been proposed to help improve both of these areas of aviation. The concept involves distributing the thrust power of a fixed wing aircraft over all or part of the wing span using few or many engines. Figure 1.1 and Figure 1.2 show two ideas that have been considered. Originally, the idea of distributed propulsion was to reduce the noise on an aircraft [23] but recently other purposes have come to light. The load redistribution reduces gust load/flutter problems and also reduces wing weight by creating passive load alleviation. There is also an improvement in safety with engine redundancy. If something happens to one of the engines, there will be less impact on thrust and control issues compared with a conventional aircraft. This concept also allows for a synergistic integration of the propulsion system with the airframe, which is a major advantage. Integrating propulsion and lift systems is an existing idea in nature: birds and flying insects use their wings to produce both thrust and lift. There may also be improved affordability with smaller, interchangeable engines. Finally and most importantly in regards to this project, there is the idea that distributed propulsion can improve propulsive efficiency. This idea was originally suggested by Kuchemann[1] in 1938 [24] with the jet-wing concept.

[1] The original reference to Kuchemann introducing the jet-wing concept has been cited to be: "On the Possibility of Connecting the Production of Lift with that of Propulsion," *M.A.P Volkenrode, Reports and Translations* No. 941 – 1 Nov., 1947, APPENDIX I, Kuchemann, D., "The Jet-wing." However, a copy of this reference could not be obtained.

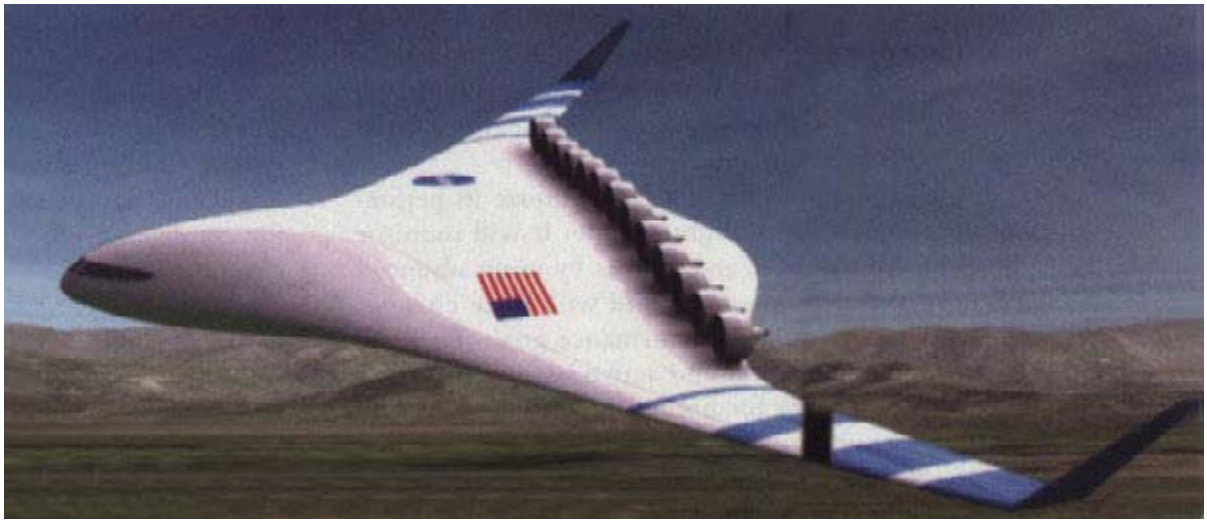

Figure 1.1: Distributed Propulsion applied to the Blended Wing Body Aircraft [22]

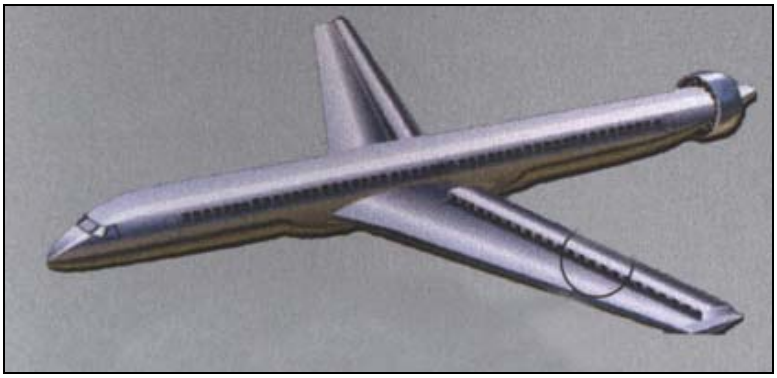

Figure 1.2: Distributed propulsion with many engines applied to a conventional transport aircraft [23].

A jet-wing distributed propulsion performance model was created by Ko [14] in his Ph.D. Dissertation in order to apply the idea to the Blended Wing Body (BWB) aircraft concept using Multidisciplinary Design Optimization (MDO). Dippold [15] began numerical studies in viscous compressible flow to validate the performance gains in Ko's jet-wing model and to help provide higher-fidelity response systems for MDO. He had some success in adding distributed propulsion to a thin airfoil with a thick trailing edge. It's important to continue with this validation to ensure that the concept can be applied in many different cases.

Distributed propulsion may help improve noise, as well as emissions, but there are many other aspects of aircraft that may also help with the noise issue.

In the last decade, the number of noise restrictions has increased by almost 100% [28]. So, studying the sources of aircraft noise is an important issue. The main components of aircraft noise are airframe noise, engine noise and engine/airframe interference noise [20]. In the past there have been many improvements made on engines so they are much quieter than they once were. It seems now that the focus has begun on improving airframe noise, which is considered the *non-propulsive* noise of an aircraft. Some of the sources include: landing gear, slats and flaps, *clean* wing, and tail surfaces. The *clean* wing (all high-lift devices and undercarriage in stowed position) is an important source of noise. For the *clean* wing, the trailing edge (TE) is the main noise device at the lower limit during approach [20]. This means that if the same lift can be obtained without using high-lift devices on approach, the *clean* wing would be the lowest bound value that can be achieved for a particular aircraft as long as there is not any massive separation on the wing. Therefore, it seems most prudent that studies involving the trailing edge noise of an aircraft be taken seriously. Some studies have been done by Hosder [20] regarding *clean* wing noise modeling for approach conditions. He developed a *noise metric*, which is an accurate relative noise measure for wings that may be used in optimizations for minimum noise. His calculations were done using a 3-D Reynolds-Averaged-Navier-Stokes (RANS) method, which is a computationally expensive way to study noise. The *noise metric* is an important concept that many would like to use in MDO. A more simplified method is desired in order to conveniently use the *noise metric* to minimize aircraft noise.

This thesis discusses some computational fluid dynamic (CFD) studies of a two-dimensional distributed propulsion model and also a simplified approach to the *noise metric* studies. The two-dimensional model for the CFD study is a representative section of the Energy-Efficient Transport (EET) Wing. The purpose of the CFD studies was to continue determining the effect a jet-wing has on the propulsive efficiency and the flowfield around an airfoil. The purpose of

the *noise metric* study was to determine the accuracy of a simplified approach compared to three-dimensional RANS calculations. The structure of this work is as follows:

- Chapter 2 reviews previous work regarding distributed propulsion, including the jet-wing and jet-flap ideas, and *noise metric* studies.
- Chapter 3 describes the set up and results obtained from the CFD calculations on a representative thick airfoil section.
- Chapter 4 explains the steps taken to derive the simplified method of the *noise metric* calculations as well as the comparison of the results with the three-dimensional studies.
- Chapter 5 presents the conclusions made from both studies.

Chapter 2: Background and Literature Review

2.1 Jet-wing and Jet Flap Concepts

The jet-wing and jet flap are two concepts that were studied as background for this research project. Both concepts use the idea of blowing a jet from the wing at or near the trailing edge, sometimes being blown over part of the airfoil. The jet-wing is associated with cruise and has the flow coming off the airfoil in the same direction as the mainstream. However, the jet flap is mainly used in high lift applications and involves a *strong, high-velocity thin jet sheet* that can be deflected like a flap [6]. The ideas behind both concepts were studied due to their similarities even though the main focus of this work is the jet-wing.

The concept of the jet-wing was first developed back in 1938 by Kuchemann as a way to improve propulsive efficiency [24]. Figure 2.1 shows a schematic of Kuchemann's concept. His idea was to bury a turbojet engine with bypass fans in the wing. The bypass ducts would not be annular like conventional fan engines but split into two cold-air ducts on either side of the gas generator. Even though Kuchemann never made a detailed assessment of his concept, he believed that even with the inevitable duct losses the jet-wing would be more efficient than the conventional arrangement of isolated engine nacelles installed outside the fuselage or wing [6].

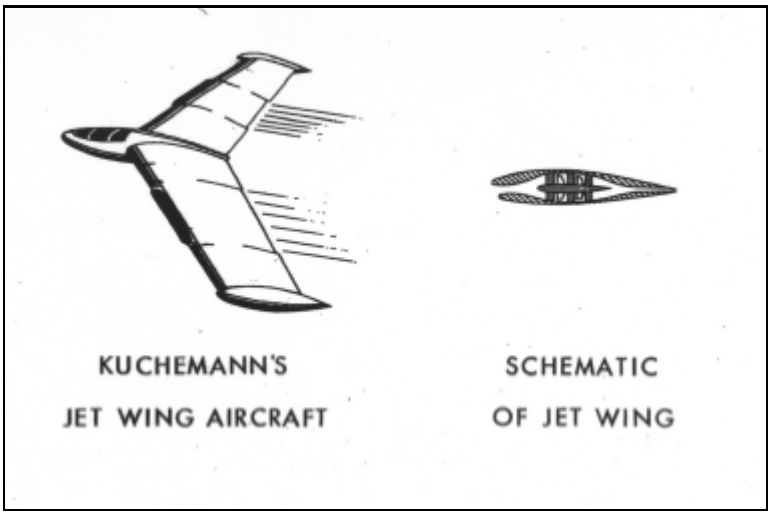

Figure 2.1: Kuchemann's Jet-wing Concept [24]

Spence developed the jet flap concept theory using inviscid, incompressible flow theory in 1956 [3]. He found an analytical solution for a thin, two-dimensional wing at small angles of attack, α, and with a jet flap also deflected at small angles, τ. Spence's theory has high-lift applications and also used jet coefficients, C_J, values larger than 1. Equation 2.1 shows the definition of the jet coefficient:

$$C_J = \frac{m \cdot U_{jet}}{\frac{1}{2} \cdot \rho_\infty \cdot U_\infty{}^2 \cdot S} \tag{2.1}$$

where U_{jet} = Jet flow velocity

m = Jet flow mass

U_∞ = Freestream velocity

ρ_∞ = Freestream density

S = Jet reference area

While this theory is only valid for small jet deflection angles, Spence showed that there was good experimental agreement for τ as large as $60°$.

Spence's theory was later extended on by Ko [14],[25]. Ko included sweep in his analysis and created a distributed propulsion model for MDO. He replaced ailerons and other moving surfaces with jet flap vectoring as a way to

control the aircraft. The concept focused on the idea of using the jet to "fill in" the wake and therefore improving the propulsive efficiency.

2.2 *Improving the Propulsive Efficiency*

The idea that Kuchemann suggested of improving the propulsive efficiency through a jet-wing sounds good in theory, but a detailed assessment needed to be made [24]. Ko began looking at the concept of the improved propulsive efficiency, which comes from the general idea of using a jet exiting the trailing edge of the wing to "fill in the wake." The design of submarines has used this idea by installing a single propeller directly behind a streamlined axi-symmetric body, neglecting the sail and control surfaces. This maximized the overall propulsive efficiency of the whole system, even though the wake is not perfectly "filled in" [27]. The jet-wing distributed propulsion concept uses these same ideas to potentially improve the propulsive efficiency for aircraft.

Equation (2.2) [26] shows the definition of the Froude Propulsive Efficiency, η_P. This is the ratio of useful power out of the propulsor to the rate of kinetic energy added to the flow by the propulsor.

$$\eta_P = \frac{T \cdot U_\infty}{q \cdot S_{ref} \cdot U_\infty \cdot \beta \cdot (\beta - 1)} \tag{2.2}$$

where T = Thrust

U_∞ = Freestream velocity

S_{ref} = Reference area

q = Dynamic pressure

β = Ratio of engine jet velocity to freestream velocity

The propulsive efficiency in Equation (2.2) can be reduced to the form given in Equation (2.3), where U_{jet} is the jet velocity.

$$\eta_P = \frac{2}{\frac{U_{jet}}{U_\infty} + 1} \tag{2.3}$$

To begin the analysis, Ko initially considered the simple two-dimensional system with a non-lifting, self-propelled vehicle with an engine as shown in Figure 2.2. This system has the wake of the body being independent of the wake of the jet from the engine. Since this system is self-propelled, the thrust of the engine exactly balances the drag associated with the velocity deficit due to the wake of the body. Any net kinetic energy, which is characterized by the non-uniformities in the velocity profile, left in the wake compared to that of a uniform velocity profile causes the loss of propulsive efficiency. For a typical high-bypass ratio turbofan engine, the Froude Propulsive Efficiency at Mach 0.85 is 80% [26].

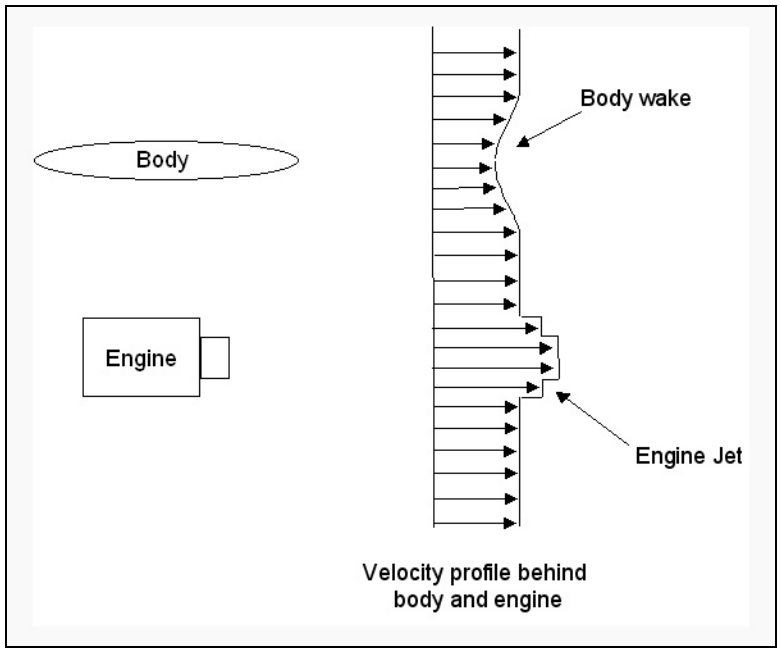

Figure 2.2: A typical velocity profile behind a body and an engine. [14]

The next step Ko took was to consider a configuration using distributed propulsion where the jet and the wake of the body are combined as seen in Figure 2.3. And ideal distributed propulsion system will have the jet perfectly "filling in the wake" and creating a uniform velocity profile. This will give a Froude Propulsive Efficiency of 100% because the kinetic energy added to the flow by the propulsor compared to that of a uniform velocity profile is zero. In actual practice, however, the wake is not perfectly "filled in" by the jet but

produces a velocity profile with smaller non-uniformities. This can be seen in Figure 2.4. This velocity profile, however, will result in a smaller net kinetic energy than the system with the body and engine separate (Figure 2.2). The distributed propulsion efficiency will be bounded by the efficiency of the body-engine system (nominally 80%) and the ideal distributed propulsion system of 100%. An analysis of the propulsive efficiency of a distributed propulsion system of this type is presented by Ko, Schetz, and Mason [25]. As a side note, the effect the jet has on the pressure distribution of the body has not been added to this simplified study. Even though it's not included in the model, the jet is expected to entrain the flow over the surface and therefore increase the drag.

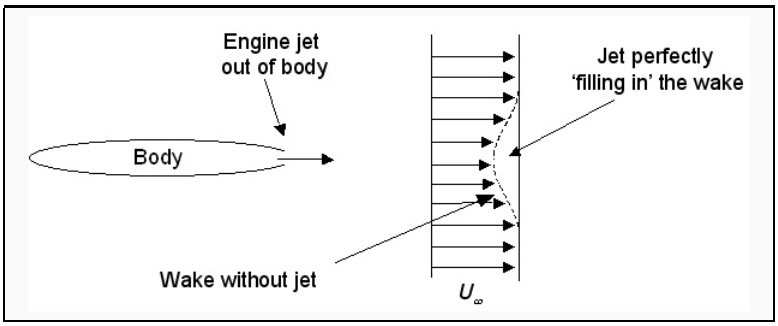

Figure 2.3: The velocity profile of a perfect distributed propulsion body/engine system [14].

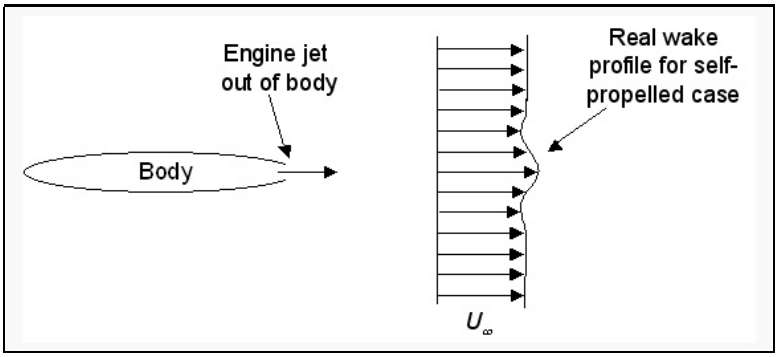

Figure 2.4: The velocity profile of a realistic distributed propulsion body/engine system [14].

The distributed propulsion concept used in this research project follows the ideas from Ko [14], [25] and Dippold [5], [15]. It is a hybrid system that ducts some of the exhaust from a high-bypass-ratio turbofan engine through the jet-wing. This approach can be seen in Figure 2.5. To overcome the drag due to the viscous and pressure forces, part of the thrust from the cold fan exhaust of the

engine is used, while the rest of the thrust is used to overcome the induced drag. Only the jet-wing portion of this hybrid approach will be discussed in this thesis, shown in Figure 2.6. The baseline used for all calculations is a propulsive efficiency of $\eta_P = 80\%$ found in Hill and Peterson [26], which will be used as a reference only because at this time there is no propulsion system that can be directly compared to the jet-wing. Since only the jet-wing portion of the hybrid system is being studied, the actual propulsive efficiency of the entire distributed propulsion system will be different from the values that will be calculated. Finally, it should be known that the baseline propulsive efficiency of $\eta_P = 80\%$ being used is only typical of the most efficient high-bypass-ratio turbofan engines. Therefore, even if the final results only show an efficiency slightly greater than 80%, it would still perform better than most systems.

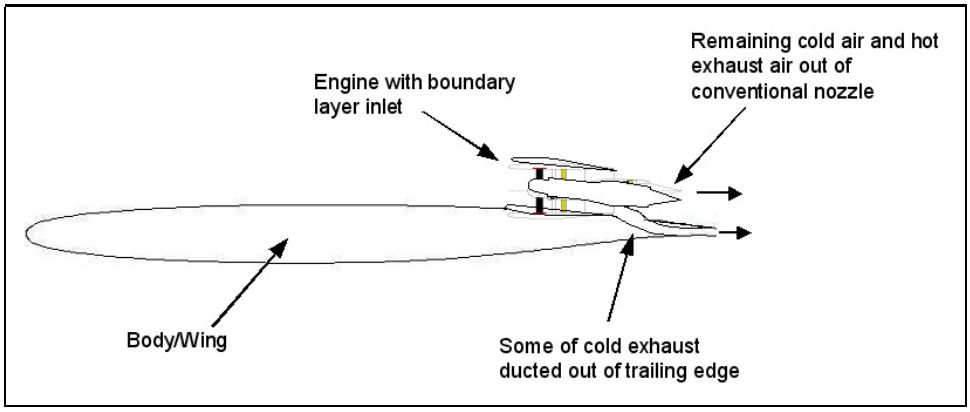

Figure 2.5: Hybrid Distributed Propulsion approach, using jet-wing and high-bypass-ratio turbofan engines [14].

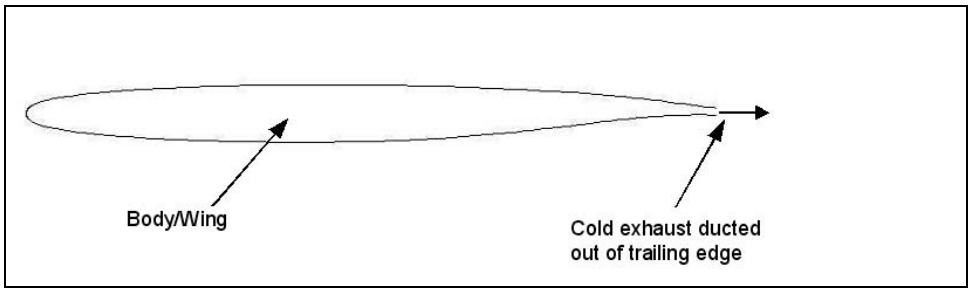

Figure 2.6: Hybrid distributed propulsion approach at a wing section without turbofan engine, where only jet-wing propulsion is present [15].

Ko's distributed propulsion system concept was used as a basis for further studies of adding distributed propulsion to wings by Vance Dippold [5],[15]. He did numerical analyses of several self-propelled jet-wing models at cruise conditions in viscous, transonic flow. His study used airfoils that were developed to be representative of a Blended-Wing Body (BWB) aircraft. The chosen representative airfoils were an "outboard" section which was a modified SC(2)-0410 airfoil that was 11% thick, had a design lift coefficient of C_L = 0.69, and a chord length of c = 6.77m, and an "inboard" section that was based on a NACA 4-digit series airfoil that was 18% thick, had a design lift coefficient of C_L = 0.30, and a chord length of c = 23.01m. The research attempted to validate the performance benefit of adding distributed propulsion to these airfoils and assess any negative consequences by performing the computational analysis using the Reynolds-averaged, three-dimensional, finite-volume, Navier-Stokes code GASP [12]. For each case, Dippold ran a case without the jet and then one adding the jet-wing. The no-jet case was used to calculate the jet characteristics for the jet-wing.

Two studies were done on the "outboard" airfoil. The first study was applying the jet-wing to the airfoil as is with a trailing edge thickness of 0.49%. This Outboard 1xTE case had an ending propulsive efficiency of $\eta_P = 75\%$. Since the height of the jet was only 0.49% of the airfoil's chord and the wake had a height of about 4% of the chord, the jet did a poor job of filling in the wake. Since the trailing edge thickness was so small and gave resultant propulsive efficiency less than the normal efficiency for a modern turbojet engine, the trailing edge thickness, and thus the jet height, was expanded to 1% of the chord. The propulsive efficiency increased to about $\eta_P = 83\%$ for the Outboard 2xTE case. Dippold determined that while this is only 3% higher than the nominal propulsive efficiency of 80%, it must be remembered that the jet-wing is only a part of a hybrid distributed propulsive system, and the propulsive efficiency of the whole system needed to be taken into account [5]. Expanding the trailing

edge did have one negative consequence, however. The drag of the Outboard 2xTE case was about 10% higher than the drag of the Outboard 1xTE case and so there are aerodynamic consequences to expanding the trailing edge thickness.

The "inboard" airfoil case CFD calculations done by Dippold [5], [15] were much more complex. His results were found to be periodic and so they lacked a true steady-state convergence, which causes problems when applying the jet-wing. The vehicle was not quite self-propelled when the jet-wing was added and so the jet velocity needed to be increased slightly, which made the propulsive efficiency around $\eta_P = 69.7\%$. However, the solution for the no-jet case for the Inboard airfoil was very different from both the design and jet cases, so the changes in the lift and, in particular, the drag could not be assessed. Dippold suggests that the airfoil design used for this Inboard airfoil case was not good and that perhaps better results could be obtained using a different baseline design. This shows that further analysis of the jet-wing distributed propulsion is needed to validate the idea that the jet-wing increases the propulsive efficiency.

2.3 *Airframe Noise Modeling*

Another focus of this thesis is creating a simplified approach to the study of airframe noise. The idea came about from the airframe noise study done by Hosder, Schetz, Grossman, and Mason [20]. This study focused on airframe noise modeling of a clean wing at approach conditions. Following the approach of Goldstein [29] and Lilley [30], [31], Hosder et al was able to create a new noise metric, which is just an accurate indicator of relative trailing edge noise, that may be used when optimizing a clean wing for minimum noise. Equation (2.4) [20] shows their equation for the Noise Metric (NM):

$$I_{NM} \approx \frac{\rho_\infty}{2\pi^3 H^2 a_\infty^{\,2}} \omega_0 u_0^{\,4} Cos^3 \beta_{TE} \qquad (2.4)$$
$$NM = 120 + 10\log(I_{NM})$$

where I_{NM} = Noise intensity indicator

ρ_∞ = Freestream density

a_∞ = Freestream speed of sound

ω_0 = Characteristic Source Frequency

u_0 = Characteristic velocity scale for turbulence

l_t = Characteristic length scale for turbulence

β_{TE} = Trailing edge sweep angle

H = Distance to the ground (receiver)

The characteristic turbulent velocity for a spanwise location of the wing trailing edge was chosen to be the maximum value of the turbulent kinetic energy (TKE) profile and the characteristic turbulence length scale for each station is the characteristic velocity divided by the turbulence frequency, ω, observed at the maximum TKE location, shown in Equation (2.5) [20].

$$u_0(y) = Max\left[\sqrt{TKE(z)}\right]$$
$$l_0(y) = \frac{Max\left[\sqrt{TKE(z)}\right]}{\omega} \tag{2.5}$$

Here, the z is the direction normal to the wing surface.

The nose metric calculations performed in that study were done using a high fidelity CFD (RANS) code using a two-equation turbulence model to obtain the characteristic length scale and velocity. The noise metric was validated using seven test cases selected from a two-dimensional NACA 0012 experimental database, which showed good agreement at various speeds and angles of attack leading to the conclusion that the noise metric is capable of capturing trailing edge noise variations as a relative noise measure [20]. Also, two supercritical airfoils (SC(2)-0710 and SC(2)-0714), along with a few others, were used in a two-dimensional parametric study that investigated the effect of lift coefficient and

wing geometry on the noise metric. These studies showed that at low lift coefficients the noise metric stays almost constant while increasing at higher lift coefficients, which can be dramatic when there is large flow separation. These CFD calculations proved that the noise metric derived by Hosder et all [20] gives an accurate measurement of trailing edge noise but these computations are quite computationally expensive. This leads to the idea that a simplified noise approach could be very useful, and that is addressed in Chapter 4:.

Chapter 3: Distributed Propulsion

3.1 Model Flow Conditions

One of the main purposes of this research project was to continue the study of distributed propulsion. Vance Dippold [15] had some success adding distributed propulsion to a thin, "outboard" airfoil (10% thick). However, he ran into some problems when dealing with a thicker, "inboard" airfoil. The "inboard" airfoil case lacked a true steady-state convergence and instead showed evidence of periodic flow. This case also showed some separation on the top surface near the trailing edge of the airfoil. This project addresses the addition of distributed propulsion to a thick, "inboard" airfoil. A decision was made to consider a realistic transonic wing. Some work had been done previously with a configuration know as an Energy-Efficient Transport (EET) wing [16]. This seemed to be a good candidate for distributed propulsion. Since there had been previous success with a thin, "outboard" airfoil, a thicker "inboard" airfoil was chosen at a span-wise location of $\eta = 0.226$ that was about 13% thick for the three-dimensional wing. The conditions studied for this configuration were the cruise conditions: Mach 0.82 at an altitude of 35,000 ft and an overall C_L value of 0.55. A Standard Atmosphere table [7] was used to establish the flow conditions at cruise, which can be seen in Table 3.1.

Freestream Mach number, M_∞	**0.82**
Freestream temperature, T_∞	**394.07 R**
Freestream pressure, p_∞	**499.4 lb/ft^2**
Freestream density, ρ_∞	**7.3653e^{-4} slugs/ft^3**
Freestream speed of sound, a_∞	**972.893 ft/s**
Freestream dynamic viscosity, μ_∞	**9.643e^{-6} lb/ft-s**

Table 3.1: Freestream Properties for the inboard EET airfoil

3.2 *Representative Wing Section*

In order to continue the task of better understanding distributed propulsion and validating analytical models, it was necessary to simplify the problem and create a representative two-dimensional wing model with this chosen Inboard EET section. The actual model of the EET wing has an inboard section at $\eta = 0.226$ with a chord length of 9.03 inches [16]. Figure 1.1 shows the inboard EET Airfoil. This needed to be scaled up to be the size of a realistic overall wing section.

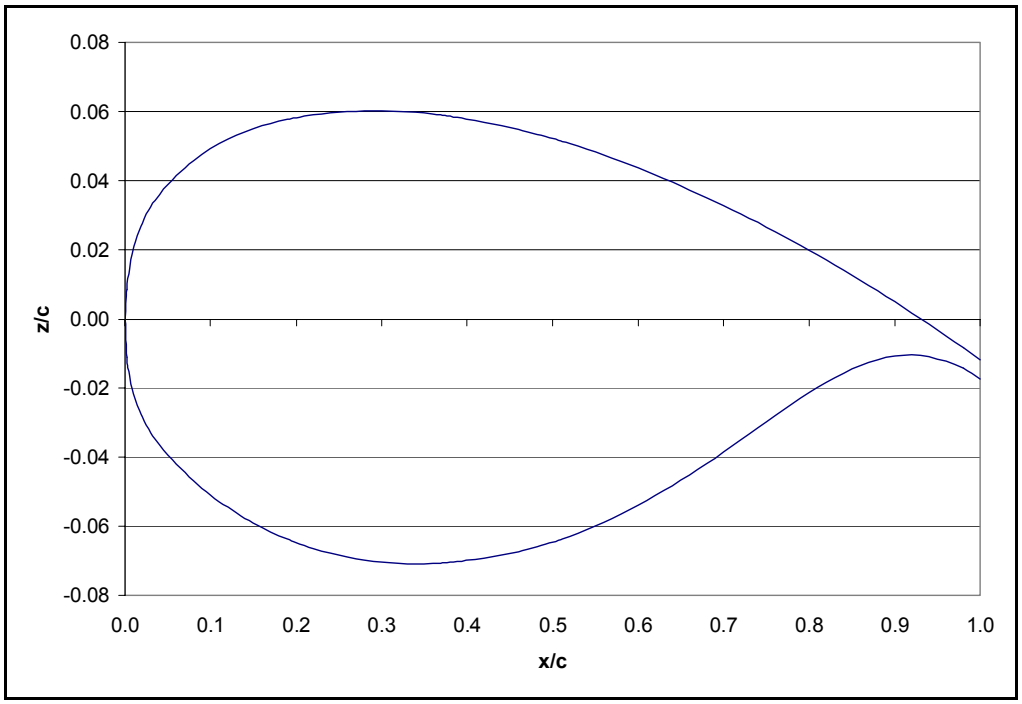

Figure 3.1: Inboard EET airfoil, $\eta = 0.226$ [16]

The scaling for the Inboard EET airfoil was done by sizing the airfoil according to the wing of a Boeing 777. A scaling factor was found by comparing the mean aerodynamic chord (MAC) of the two wings. The MAC of the EET Wing was found to be 5.74 inches according to [16] and using a drawing found on the Boeing Website [19], the MAC for the 777 was found to be 30.37 ft. This led to a scaling factor of 63.49 giving the actual chord length of the Inboard EET airfoil to be approximately 47.77 ft.

Since the CFD model that is being used will be two-dimensional and the conditions in Table 3.1 were for the 3-D case, the corresponding 2-D values needed to be found. Simple Sweep Theory [17] was used to get the 2-D Mach number from the 3-D value using the EET Wing's quarter-chord sweep of 35°. The following equations were used:

$$\begin{aligned} c_{2D} &= c \cdot \cos\left(\Lambda_{1/4}\right) \\ M_{2D} &= M_{\infty} \cdot \cos\left(\Lambda_{1/4}\right) \\ C_{L_{2D}} &= \frac{C_L}{\left(\cos\left(\Lambda_{1/4}\right)\right)^2} \\ \left(\frac{t}{c}\right)_{2D} &= \frac{\left(t/c\right)_{streamwise}}{\cos\left(\Lambda_{1/4}\right)} \end{aligned} \tag{3.1}$$

where $\Lambda_{1/4}$ is the quarter chord sweep. The results can be seen in Table 3.2.

	3-D	2-D
¼-chord sweep, $\Lambda_{1/4}$	**35°**	**--**
Chord, c	**47.77 ft**	**39.13 ft**
Thickness, $\frac{t}{c}$	**13.06%**	**16%**
Lift Coefficient, C_L	**0.55**	**0.82**
Freestream Mach number, M_{∞}	**0.82**	**0.67**

Table 3.2: 2-D and 3-D Characteristics of the Inboard EET airfoil

3.3 MSES Flow Solver

The multi-element airfoil analysis code MSES [8], [9] was used to assist in the analysis of the Inboard EET Airfoil. The steady Euler equations are solved in MSES by coupling a finite-volume method on an "intrinsic streamline grid" in the inviscid region with an integral boundary layer method in the viscous region [9]. Most importantly, MSES can solve flows with some separation and transonic flows that contain shocks. The input into to MSES is simply the airfoil

coordinates, Mach number, Reynolds Number, lift coefficient or angle of attack and a few grid parameters. The solution can be found for a specified lift coefficient or angle of attack. MSES can solve flow problems in just a few minutes on an SGI workstation, which makes the process computationally inexpensive and appealing to use. The output of MSES includes the following: surface pressure distribution, lift and drag coefficients, angle of attack, flowfield quantities and boundary layer properties. The short computation time and ease of use made MSES a good first analysis of the Inboard EET airfoil.

3.3.1 MSES Results

A number of MSES runs were made in order to obtain the best run conditions for the Inboard EET airfoil model. The MSES calculations are much less computationally expensive than full GASP runs and so it seemed prudent that the best flowfield conditions be known before making the CFD computations.

The first MSES run was made using the 2-D conditions determined previously from the 3-D values, see Table 3.2. Figure 3.2 and Figure 3.3 show the pressure and skin friction distributions from MSES obtained from this run, respectively. The pressure distribution appears to give credence to the fact that these conditions would give a viable run in GASP. However, the skin friction distribution shows that there is some separation occurring before the flow transitions from laminar to turbulent on the top surface.

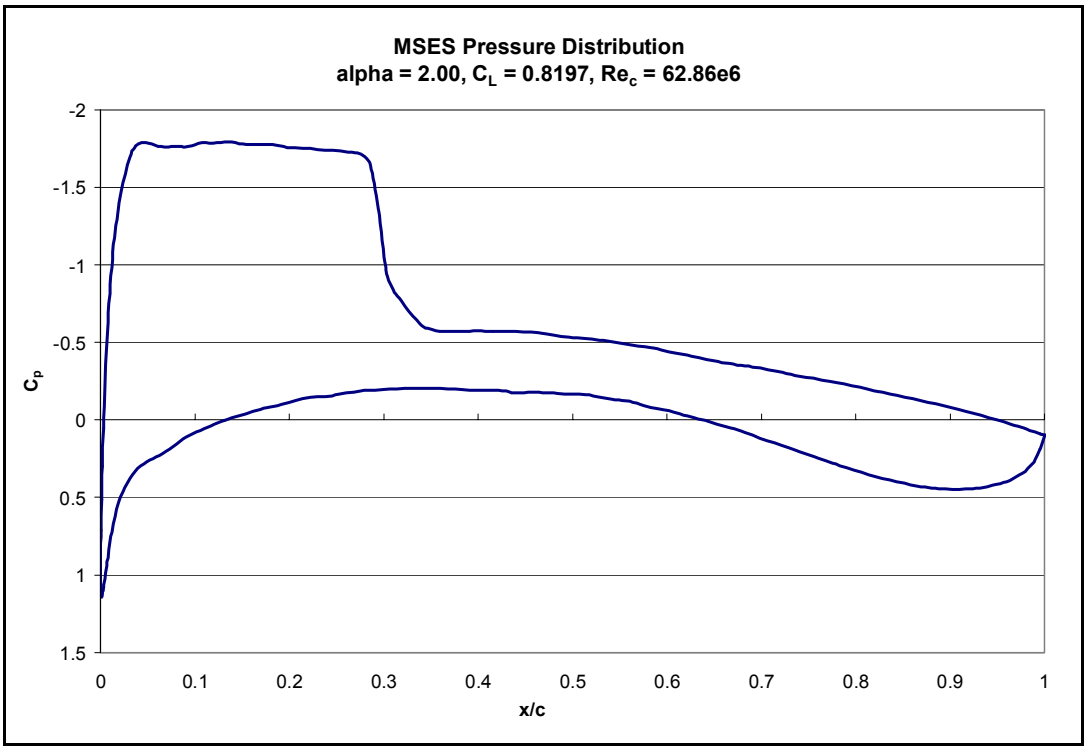

Figure 3.2: MSES Pressure Distribution for inboard EET airfoil

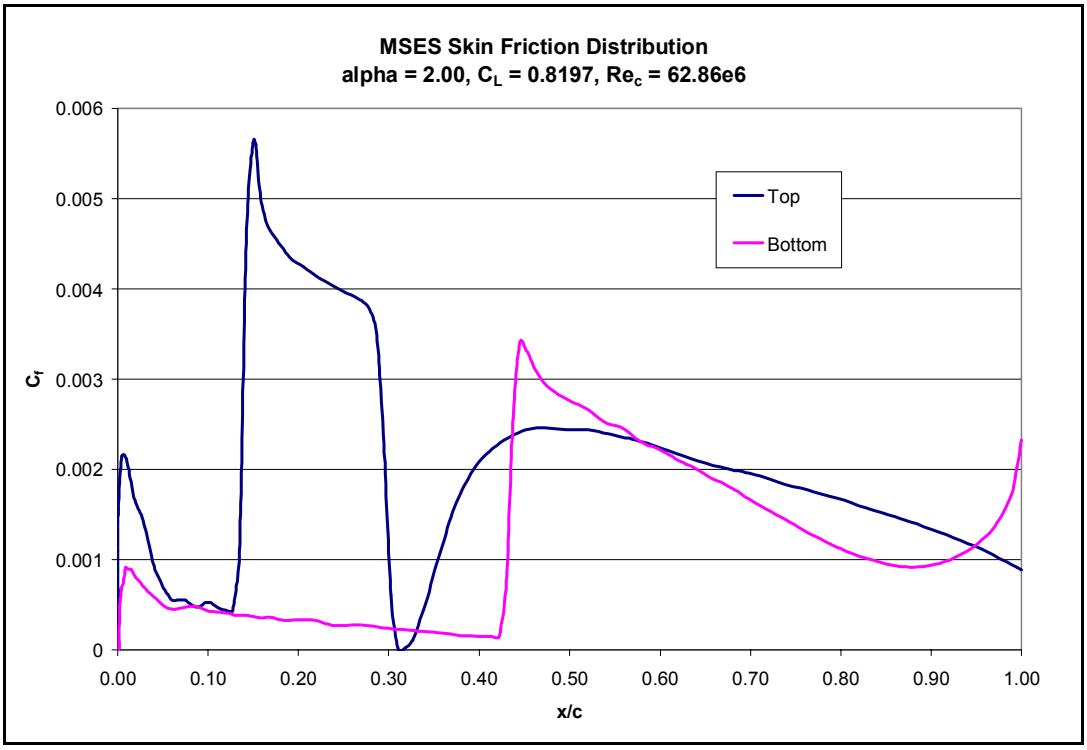

Figure 3.3: Skin Friction Distribution for inboard EET airfoil

Taking into consideration the separation on the top surface of the airfoil, it was decided to see if there was any current data available on the inboard EET airfoil for comparison purposes. A paper by Allison and Cavallo [18] gave some pressure distributions for different span stations of the EET Wing. Figure 3.4 shows two pressure distributions for span stations close to that of the Inboard EET airfoil ($\eta = 0.226$). The pressure distribution for this case should look similar to a mix between these two distributions.

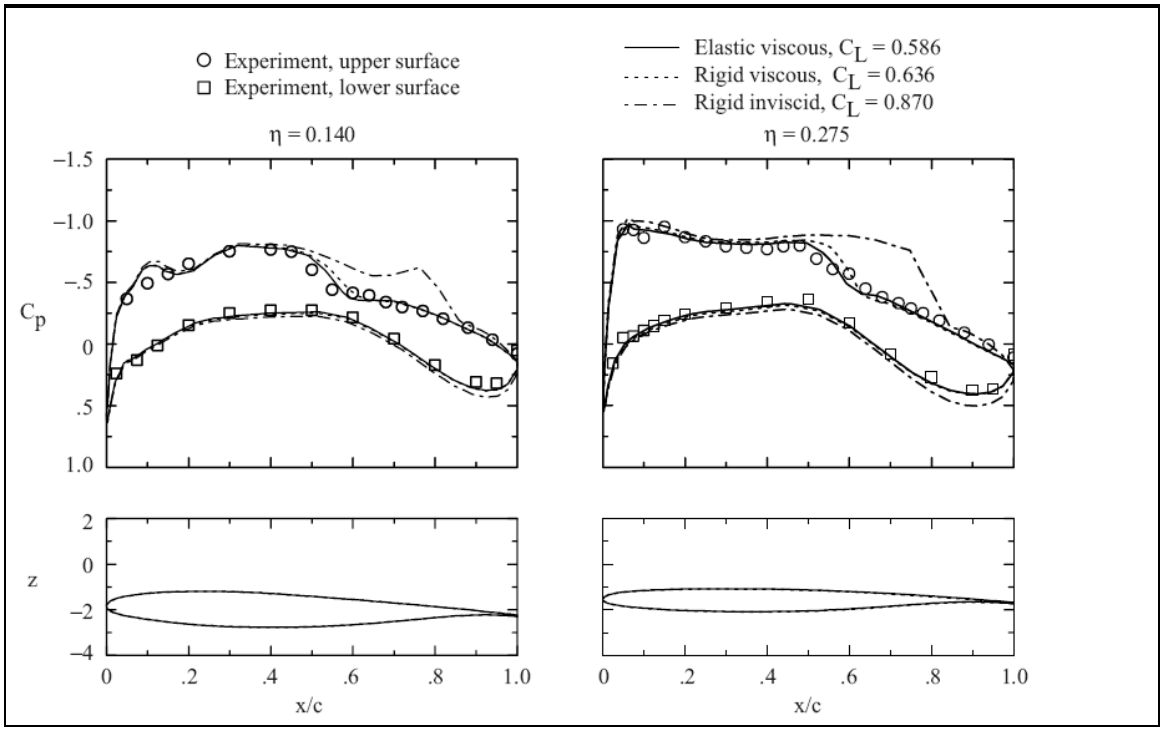

Figure 3.4: Pressure Distributions from Allison and Cavallo [18]

The pressure distribution found by MSES doesn't appear to be close to either of these two pressure distributions, so it was decided that a parametric study should be made to find a Mach number and C_L combination that will give a pressure distribution that is similar to those from Allison and Cavallo [18].

Six different MSES cases were run in order to obtain a viable pressure distribution. The cases can be seen in Table 3.3. The first three runs held the C_L constant and changed the Mach number where as the last three cases kept the Mach number constant and changed the C_L.

Case	Mach No.	C_L
1	0.67	0.82
2	0.70	0.82
3	0.65	0.82
4	0.67	0.62
5	0.67	0.73
6	0.67	0.90

Table 3.3: inboard EET airfoil Cases run in MSES

The first case is just the original values found from Simple Sweep Theory, the results of which can be seen in Figure 3.2 and Figure 3.3. Figure 3.5 through Figure 3.14 show the pressure and skin friction distributions for the other 5 cases.

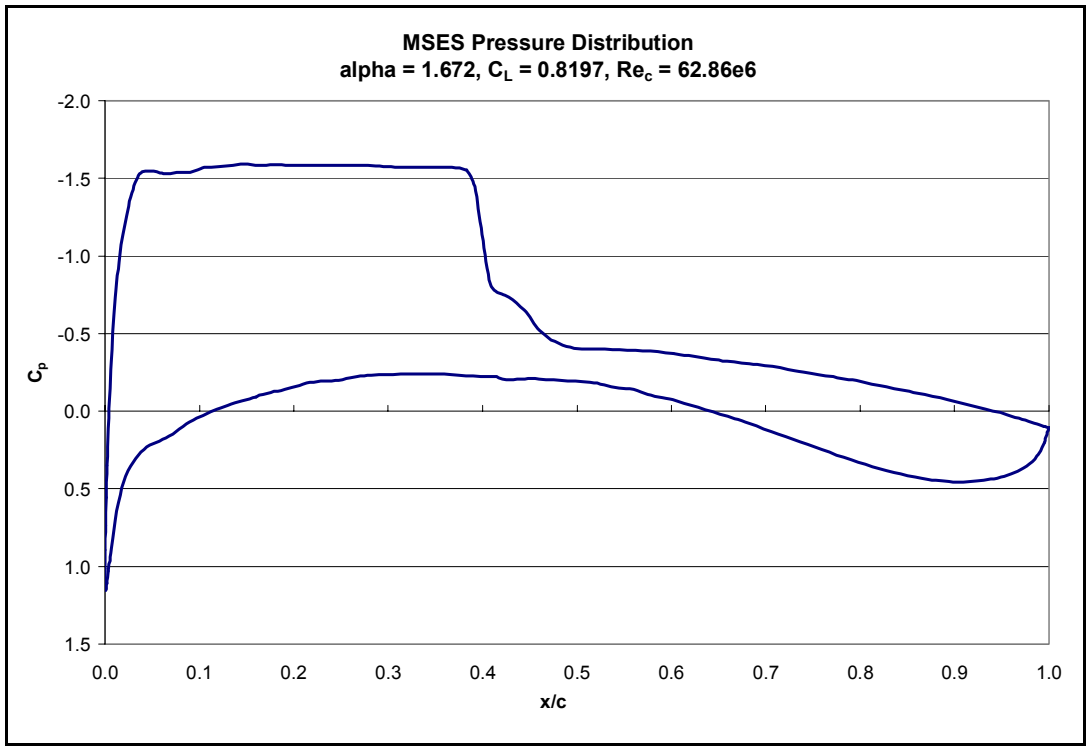

Figure 3.5: Pressure Distribution for Case 2

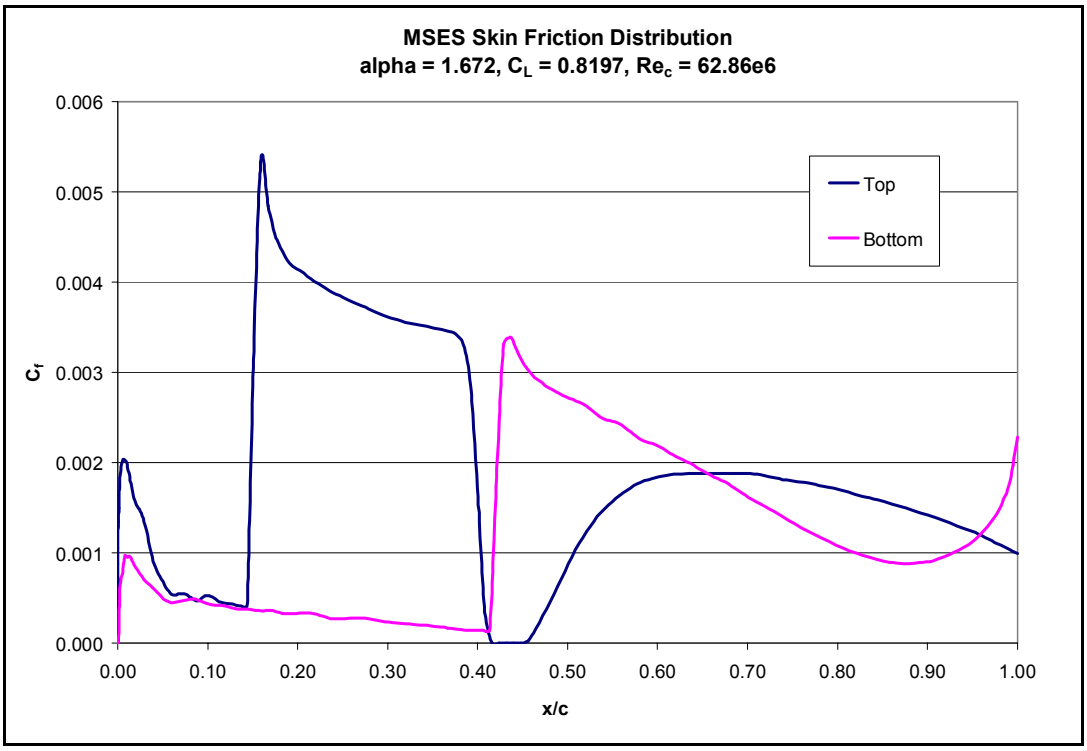

Figure 3.6: Skin Friction Distribution for Case 2

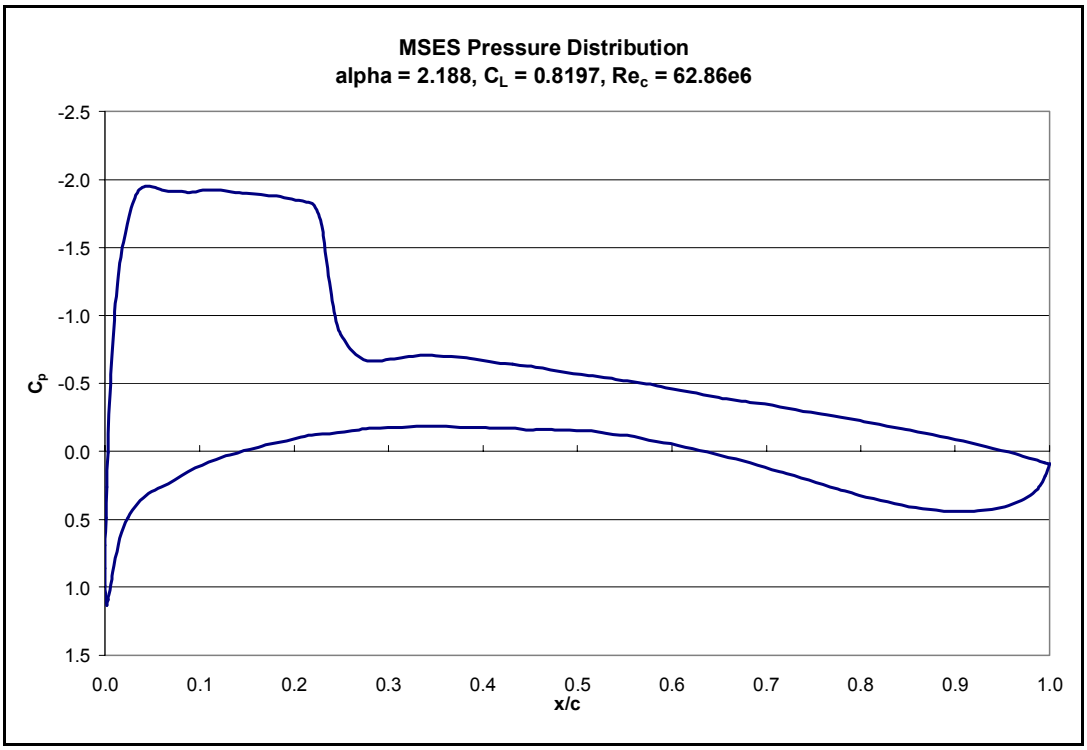

Figure 3.7: Pressure Distribution for Case 3

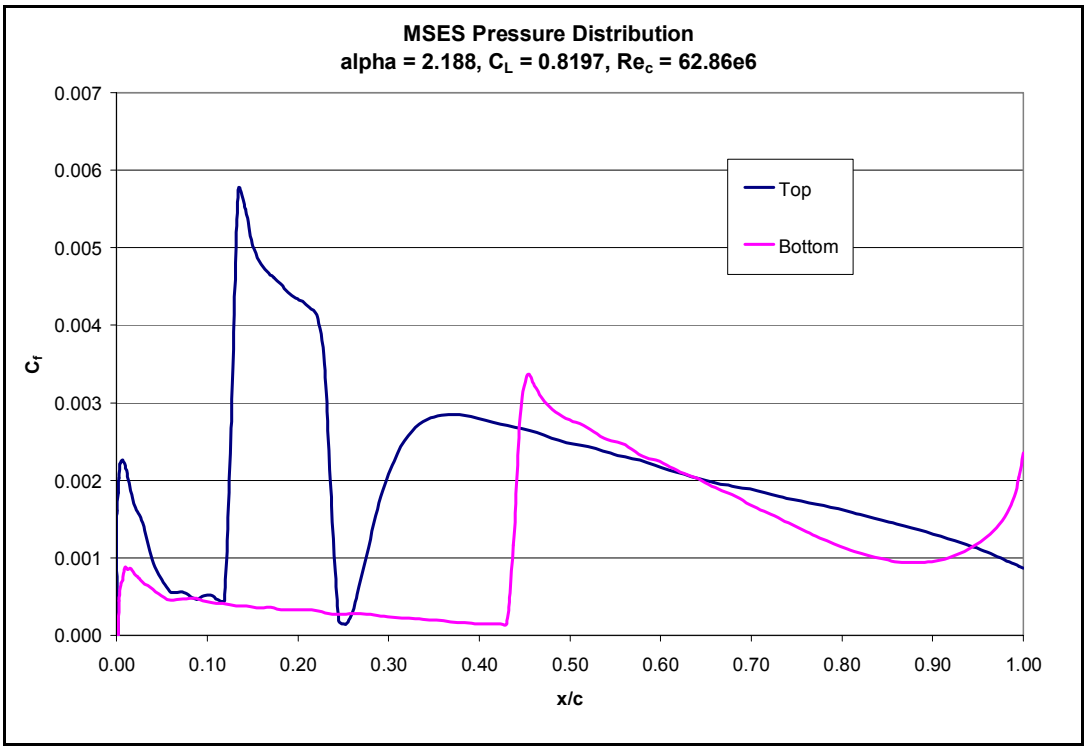

Figure 3.8: Skin Friction Distribution for Case 3

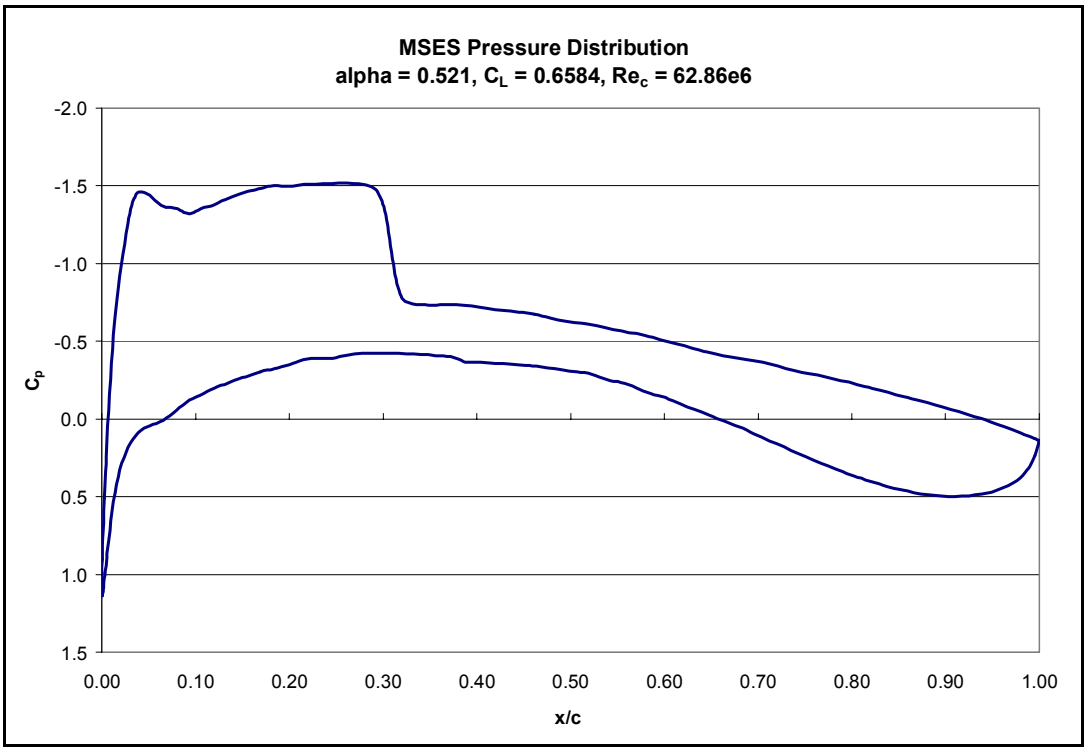

Figure 3.9: Pressure Distribution for Case 4

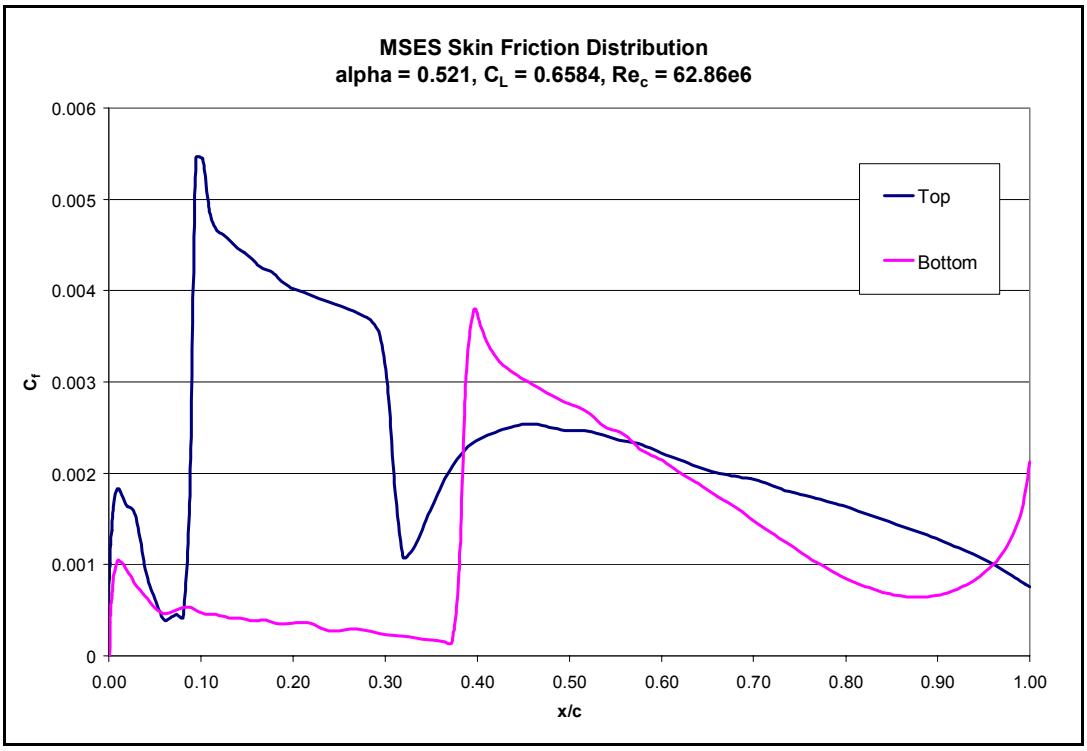

Figure 3.10: Skin Friction Distribution for Case 4

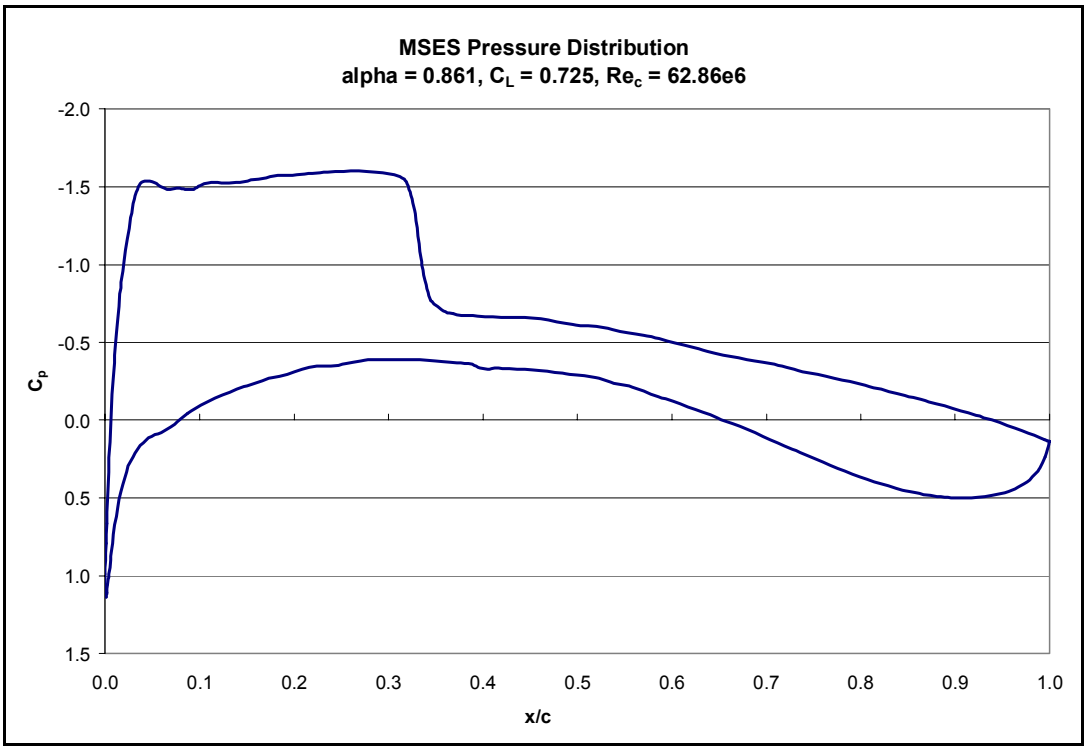

Figure 3.11: Pressure Distribution for Case 5

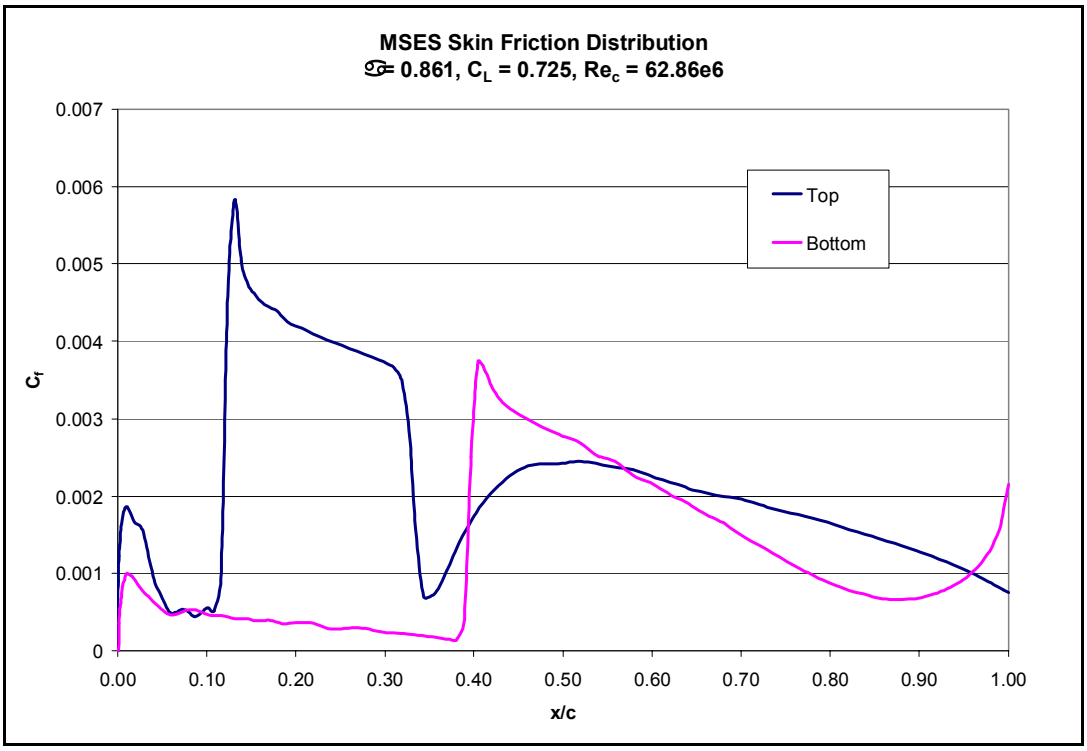

Figure 3.12: Skin Friction for Case 5

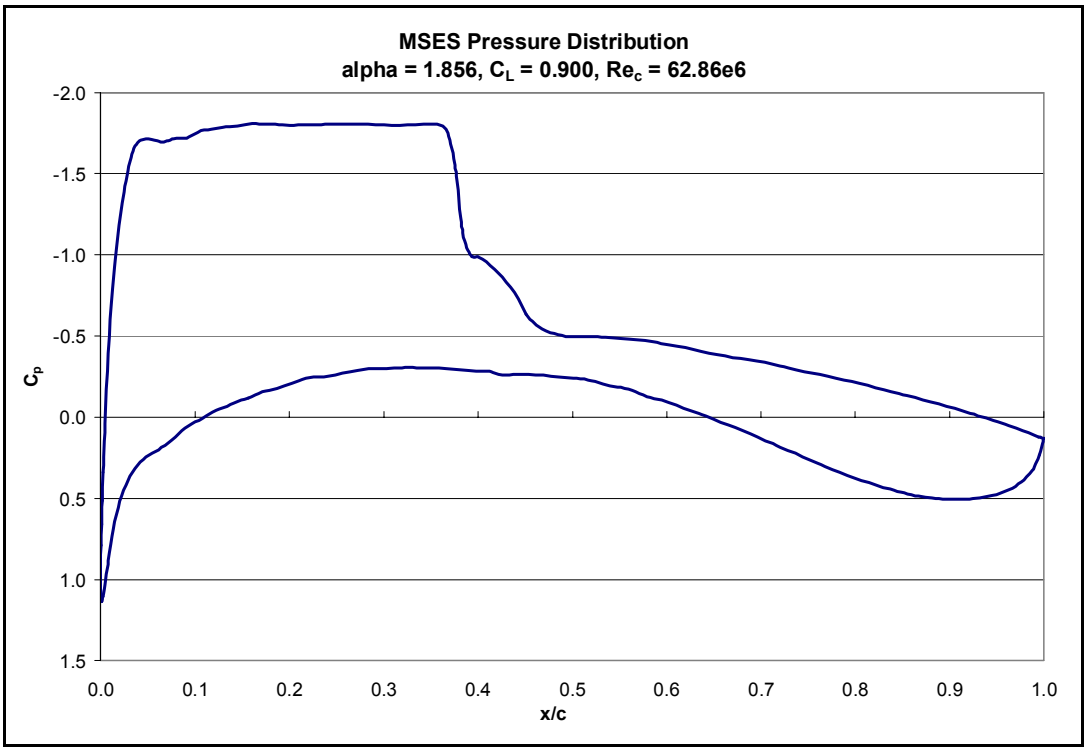

Figure 3.13: Pressure Distribution for Case 6

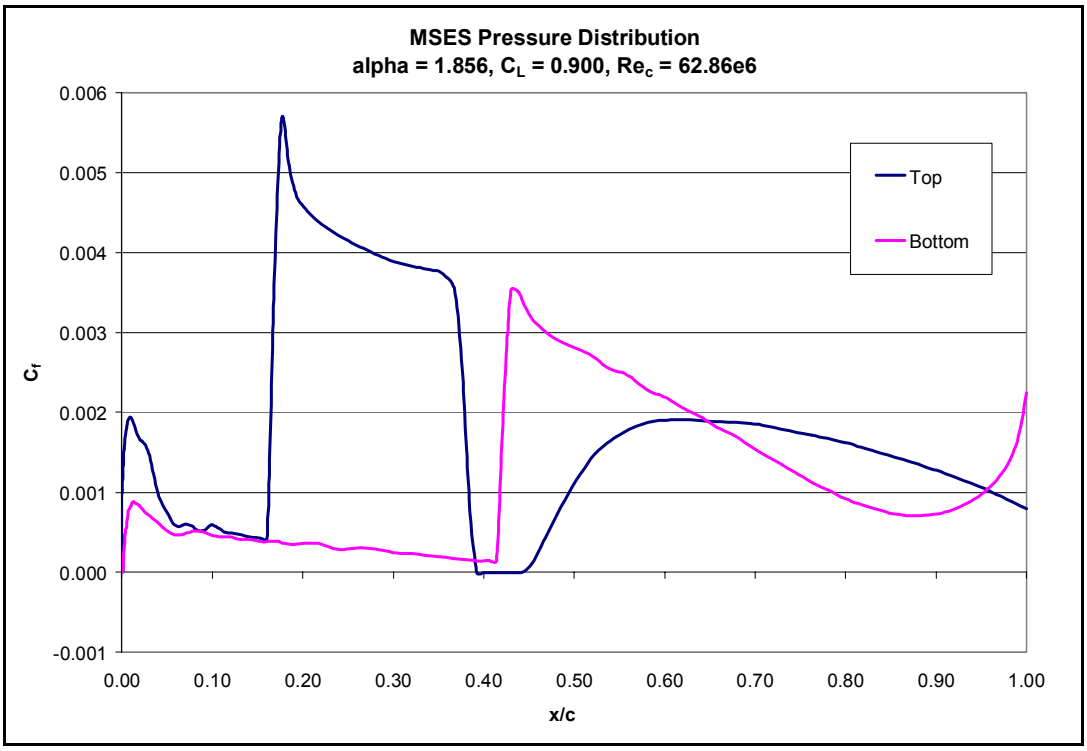

Figure 3.14: Skin Friction Distribution for Case 6

These plots show that many of the cases studied came very close to separation, or separation occurred along the top surface of the airfoil. These cases were quickly dismissed. This left just cases 4 (Figure 3.9 and Figure 3.10) and 5 (Figure 3.11 and Figure 3.12) to be studied further. Comparing their pressure distributions to Figure 3.4, they both have similar properties as the distributions from Allison and Cavallo [18], however, case 4 seemed to be the closest and was also the furthest from separation. So it was decided that the flow conditions from this case would be the conditions used to make the full CFD calculations using the GASP software.

3.4 GASP Modeling of Jet-wing

The Reynolds-averaged, three-dimensional, finite-volume, Navier-Stokes code GASP [12] has been used by many in the Aerospace and Ocean Engineering Department at Virginia Tech. Graduate Student Vance Dippold [15] was the first to use GASP to model distributed propulsion. Applying the concept of the jet-

wing to distributed propulsion allowed him to use GASP in making his Computational Fluid Dynamic (CFD) calculations.

3.4.1 Grid Generation for Inboard EET Airfoil

The commercially available software Gridgen Version 14 [12] was used to create the grid for the Inboard EET airfoil. Since GASP uses a structured finite volume method to solve the three-dimensional, Navier-Stokes equations, a structured C-grid was constructed. This airfoil was modeled with the full chord length of 39.13 ft. Figure 3.15 shows the basic geometry of the C-grid. This geometry follows the set up of the grids used by Dippold [15]. The grid extends over 25 chord lengths in the positive and negative y-direction and 33 chord lengths in the positive x-direction. Again, following the steps of Dippold [15], the grid was split into two zones due to the thickness of the trailing edge of the airfoil. The first zone, labeled the "Trailing Edge Zone," extends from the trailing edge of the airfoil to the down stream grid boundary and the second zone is labeled the "Airfoil Zone," which encloses both the airfoil and the trailing edge zone. The Inboard EET airfoil is very thick (~ 16%) and also highly cambered near the trailing edge, so 325 points were placed on both the top and bottom of the airfoil. Since the trailing edge of the airfoil is thick, 81 points were placed along it and 85 were placed along the trailing edge zone. The points at the leading and trailing edge of the airfoil and at the beginning and end of each side of the trailing edge zone were spaced according to Table 3.4. The rest of the grid points were spaced using a built-in hyperbolic tangent spacing function. To create the airfoil zone, the upper and lower surfaces of the airfoil along with the shared trailing edge zone edges were extruded. The grid spacing away from the surface was determined by a hyperbolic tangent function. To make sure that some grid points were located in the laminar sublayer, it was necessary to ensure that the first grid point was located near a y^+ value of 1. Using equation 3.2 from

The Handbook of Grid Generation [21], it was found that the initial grid spacing needed to be 2 x 10^{-5}.

$$\Delta y_{physical} = \left(\frac{c \cdot y^{+}}{\mathrm{Re}_c}\right) \cdot \left(\frac{\upsilon_{wall}}{\upsilon_{\infty}}\right) \cdot \sqrt{\left(\frac{\rho_{wall}}{\rho_{\infty}}\right) \cdot \frac{2}{C_f}} \qquad (3.2)$$

$$C_f = 0.025 \cdot \left(\mathrm{Re}_c\right)^{-\frac{1}{7}}$$

The grid was extruded away from the surface of the airfoil 64 steps using smoothing parameters that can be seen in Table 3.5. The trailing edge zone is rectangular, so Gridgen extruded this automatically from an edge using the grid points along each.

The grid created for the Inboard EET airfoil is a two-dimensional grid where as GASP is a three-dimensional solver. Therefore, it was necessary to extrude the whole grid one step (one chord length) in the z-direction. This gives the model two points in the z-direction which is all that is necessary for our model. The final grid is shown in Figure 3.16, Figure 3.17 and Figure 3.18.

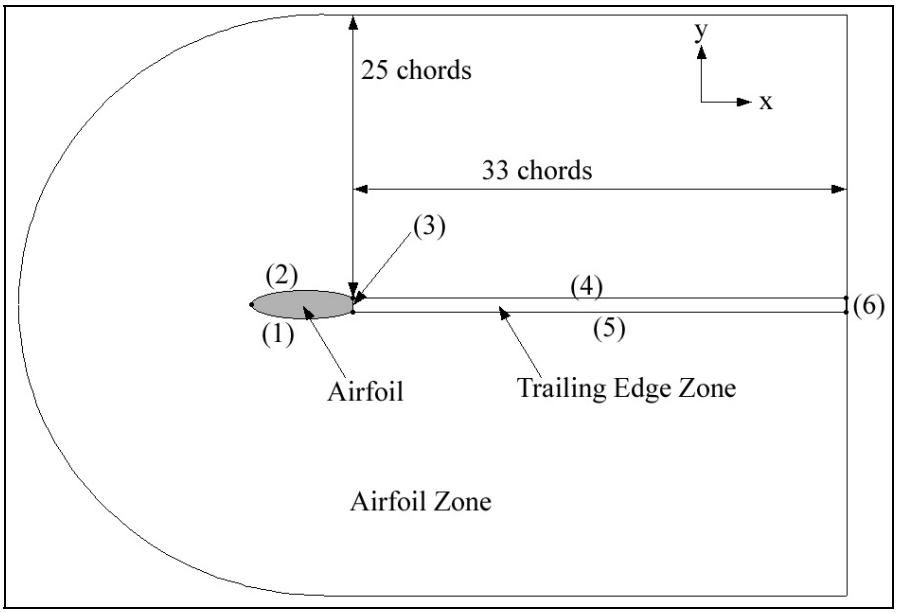

Figure 3.15: General airfoil grid geometry and nomenclature

Gridgen Edge	Number of Grid Points	Beginning Step Size	Ending Step Size
(1) Airfoil Lower Surface	**325**	**2.00E-04**	**2.00E-05**
(2) Airfoil Upper Surface	**325**	**2.00E-04**	**2.00E-05**
(3) Airfoil Trailing Edge	**81**	**2.00E-06**	**2.00E-06**
(4) Trailing Edge Zone Upper Edge	**85**	**2.00E-05**	**----**
(5) Trailing Edge Zone Lower Edge	**85**	**2.00E-05**	**----**
(6) Trailing Edge Zone Outlet	**81**	**2.00E-06**	**2.00E-06**

Table 3.4: Inboard EET airfoil grid spacing (see Figure 3.15)

Extrusion Step	**1**	**2**	**3**	**4**	**5**	**6**
Number of Steps	20	20	10	4	5	5
Explicit	0.5	0.5	0.5	0.5	0.5	0.5
Implicit	1.0	1.0	1.0	1.0	1.0	1.0
Volume	0.0	0.0	0.2	0.3	0.3	0.5
Kinsey-Barth	3.0	2.0	1.0	1.0	0.0	0.0
Geometric Growth Rate Factor	1.35	1.35	1.35	1.35	1.35	1.35

Table 3.5: Inboard EET airfoil Gridgen extrusion smoothing parameters for Airfoil Zone

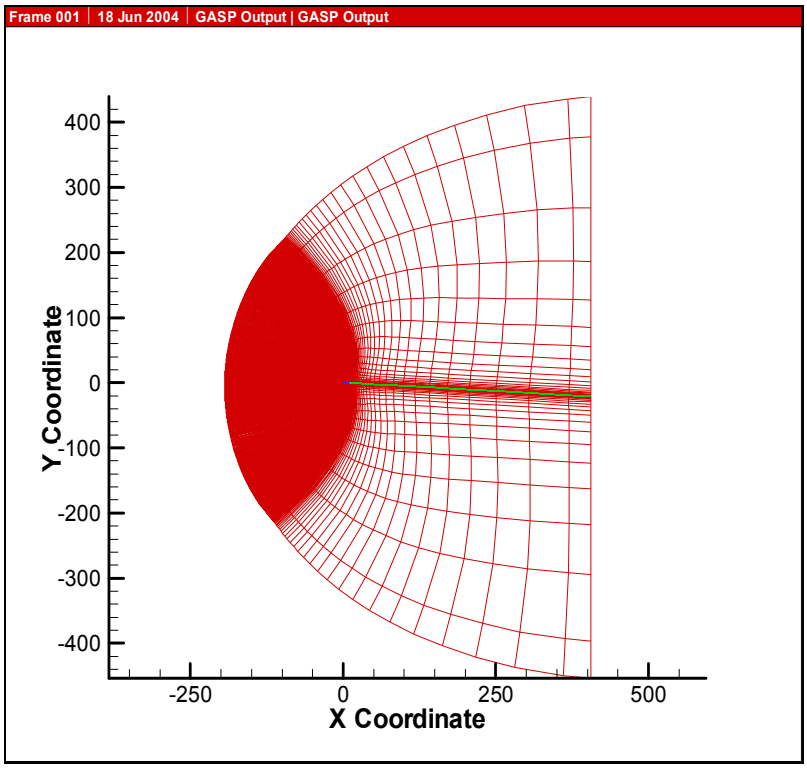

Figure 3.16: Computational Grid for the inboard EET airfoil

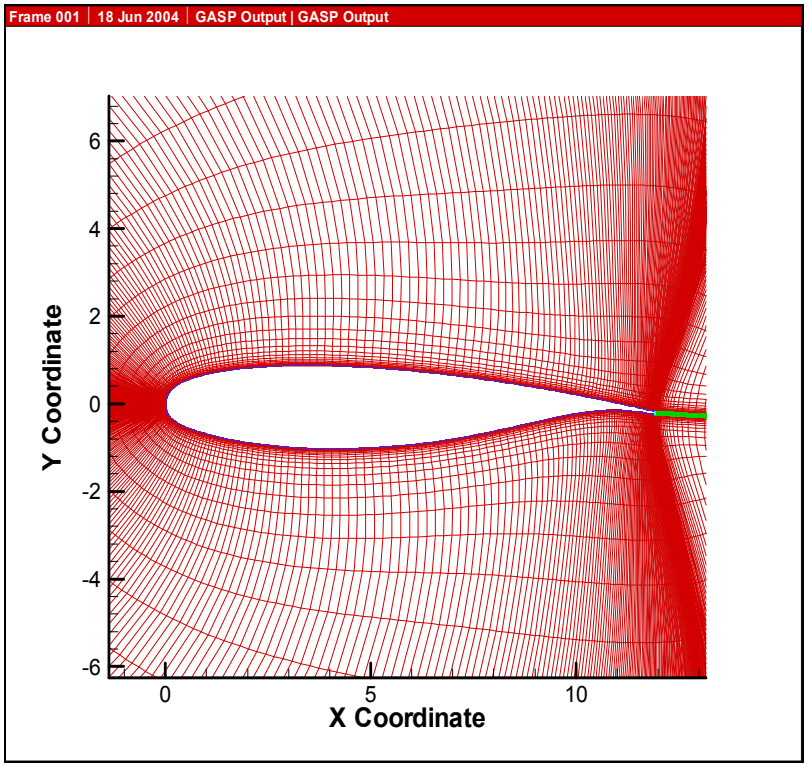

Figure 3.17: Close up of the grid around the inboard EET airfoil

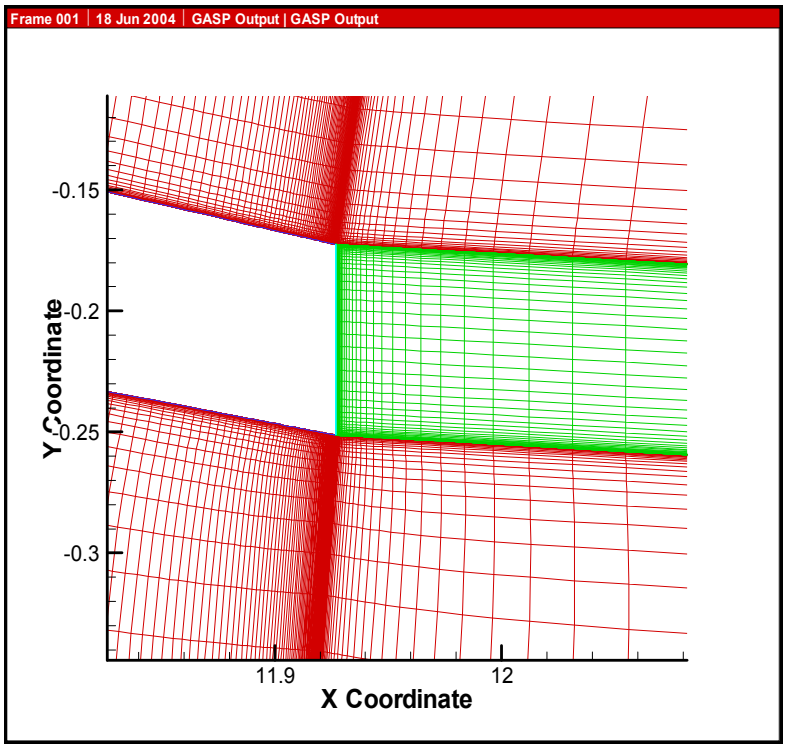

Figure 3.18: Close up of grid near the trailing edge of the inboard EET airfoil

3.4.2 GASP Input

To analyze the two-dimensional model of the Inboard EET airfoil, GASP Version 4.1.1 was used. This three-dimensional Navier-Stokes code has many input parameters that must be set up before any cases can be run. The next few sections will define the parameters used to analyze the model.

3.4.2.1 Surface Definitions

To begin, the grid that was created in Gridgen was imported into GASP. In creating the grid, English Units were used and so when importing the grid it was important to specify the units as English. Once imported, the surfaces needed to be defined. The surfaces were defined following the process used by Dippold [15]. Figure 3.19 shows the definitions of each surface. The two zones have some surfaces where the points are linked along the surfaces and share their properties; these were defined as point-to-point surfaces.

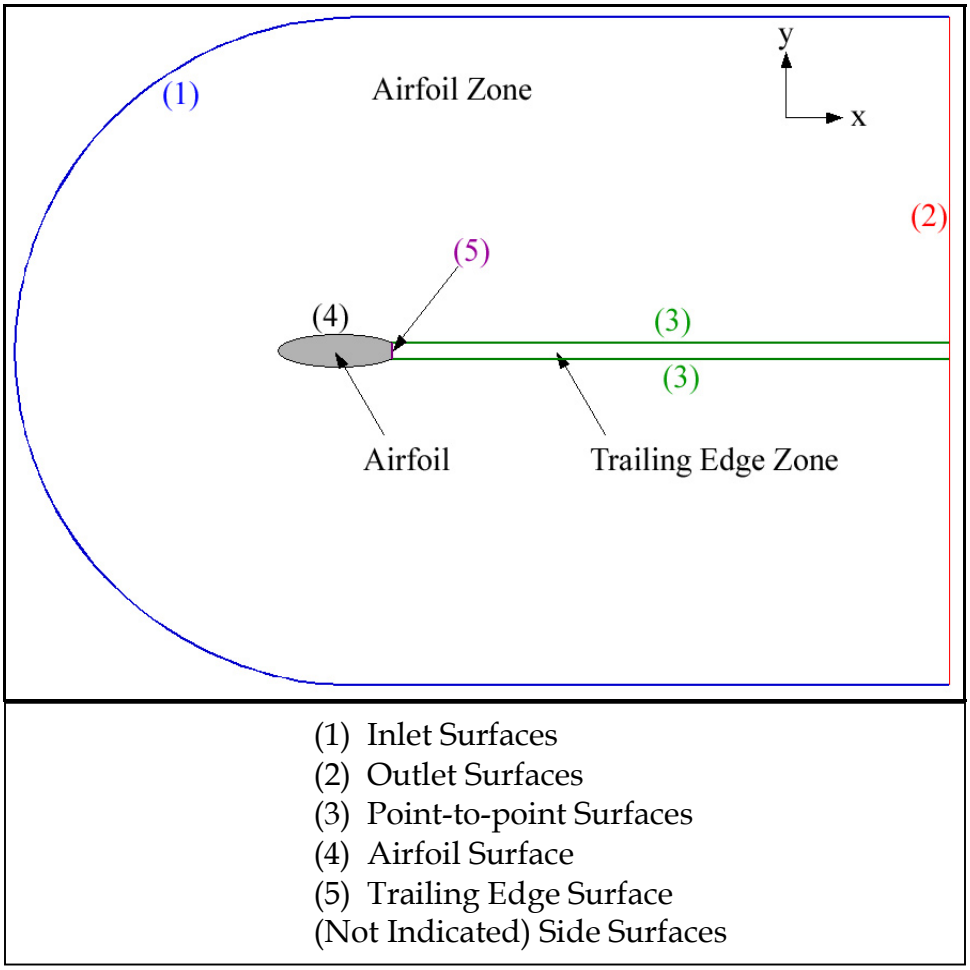

Figure 3.19: Definitions of GASP surfaces

3.4.2.2 Grid Levels and Sequences

The original grid that was imported from Gridgen is a very fine grid and if one were to run that grid alone, it would take a very long time to converge. Therefore, it is prudent to coarsen the grid and have that grid converge first to help decrease the amount of CPU time. In running this model, three grids were used: a fine grid, a medium grid and a coarse grid. To create the medium grid, every other i and j point of the fine grid in the *x-y* plane was removed. This makes the medium grid half as fine as the fine grid in all directions. In a similar manner, every other i and j point of the medium grid in the *x-y* plane were

erased to create the coarse grid, making it a quarter as fine as the fine grid. This makes the coarse grid have $1/16^{th}$ the number of cells as the fine grid, allowing this grid to converge much quicker. Once the coarse grid was converged, the solution was then interpolated to the medium grid to be used as the initial solution. Again to help with convergence, the medium grid was converged and then interpolated as the initial solution to the fine grid.

3.4.2.3 Freestream Properties

The next step in setting up the CFD run was to input the physical properties and models needed into GASP. These include the freestream and jet flow properties, inviscid and viscous models, and the boundary conditions. The temperature, density, Mach number and angle of attack needed to be set for the freestream and jet flow properties. No scaling was needed because the actual cord length (39.13 ft) was used in creating the grid. The flow direction vector was designated by using the angle of attack in Equation 3.3. Table 3.6 shows the freestream values for the Inboard EET airfoil.

$$\begin{aligned} \hat{U}_x &= Cos(\alpha) \\ \hat{U}_y &= Sin(\alpha) \\ \hat{U}_z &= 0 \end{aligned} \tag{3.3}$$

Freestream Mach Number, M_∞	0.67
Freestream Temperature, T_∞	394.07 $^\circ R$
Freestream Density, ρ_∞	7.387E-04 slugs/ft^3
Angle of Attack, α	0.521°
x-comp. of Flow Direction, $\hat{U}_x$	0.999959
y-comp. of Flow Direction, $\hat{U}_y$	0.009093
Reynolds Number, Re_c	62.86E+6

Table 3.6: Freestream Properties for inboard EET airfoil

3.4.2.4 Jet Flow Properties

The no-jet airfoil case results were used to determine the jet properties. It was assumed that the jet would use cold exhaust from the engine fan and thus would be at the same temperature as the freestream. The pressure was taken to be the average of the pressures on the upper and lower trailing edge surfaces of the airfoil. The density is the actual input into GASP so it was then calculated using the ideal gas law. Therefore, the jet Temperature, T_{jet}, and density ρ_{jet}, were calculated using equation 3.4, where R is the gas constant of air.

$$\begin{aligned} T_{jet} &= T_\infty \\ p_{jet} &= \tfrac{1}{2}\cdot\left(p_{TE_{upper}} + p_{TE_{lower}}\right) \\ \rho_{jet} &= \frac{p_{jet}}{R\cdot T_{jet}} \end{aligned} \qquad (3.4)$$

The thrust of the jet was used to determine the jet Mach number, M_{jet}. Dippold [15] showed that since the jet-wing is locally self-propelled, the jet thrust component in the freestream direction is equal to the drag and after some manipulating, he obtained the following equation:

$$\frac{C_D\cdot\left(\frac{1}{2}\cdot\rho_\infty\cdot U_\infty^2\cdot c\cdot b\right)}{Cos(\alpha+\tau)} = \rho_{jet}\cdot U_{jet}\cdot h_{jet}\cdot\left(U_{jet}-U_\infty\right)+\left(p_{jet}-p_\infty\right)\cdot h_{jet} \qquad (3.5)$$

In equation 3.5, C_D is the drag coefficient, c is the chord length and b is the span which is taken to be 1 ft. Also, U_{jet} is the jet velocity, h_{jet} is the jet height, and τ is the jet angle relative to the chord line. The equation solvers in *Mathematica* were used to solve for U_{jet} in Equation 3.5. The speed of sound for both flows was equal since the temperature was the same for both the freestream and jet. Therefore, the jet Mach number was found from the following:

$$a_{jet} = a_{\infty}$$
$$M_{jet} = \frac{U_{jet}}{a_{jet}} \tag{3.6}$$

Table 3.7 shows the jet properties for the Inboard EET airfoil.

Drag Coefficient, C_D	0.0118
Jet Mach Number , M_{jet}	1.059
Jet Temperature, T_{jet}	394.07 R
Jet Density, ρ_{jet}	7.3851e^{-4} slugs/ft^3
Jet Angle, τ	3°
x-comp. of Flow Direction, $\hat{U}_x$	0.99863
y-comp. of Flow Direction, $\hat{U}_y$	0.052336

Table 3.7: Jet properties for the inboard EET airfoil

3.4.2.5 Boundary Conditions

All surfaces in the computational domain, those indicated in Figure 3.19 including the two "side" surfaces (those parallel with the paper), needed to have boundary conditions specified for them. The inlet and outlet surfaces have a Riemann subsonic inflow/outflow boundary condition applied using the freestream values in Table 3.6 with flux splitting enabled on these surfaces. The "side" surfaces also have flux splitting enabled but with a first-order extraction boundary condition. The airfoil surface has a no-slip, adiabatic boundary condition with flux splitting disabled. For the no-jet airfoil cases, the trailing edge surface has the same no-slip, adiabatic boundary condition as the airfoil surface.

The trailingeEdge surface boundary condition is changed for the cases with the jet-wing since there is a jet exhausting from this surface. The boundary conditions at the trailing edge were set to Fixed-Q (No Turbulence) using the jet properties shown in Table 3.7. In GASP [12], Q is defined as the set of variables used to specify the flow conditions, which include velocity, temperature, pressure, density, laminar and turbulent viscosities, and Mach number. Hence, the set of parameters specifying the free stream conditions is Q_∞ and the set of parameters of an individual cell is Q_{local}. Flux splitting is disabled along the surface. This boundary condition is adequate for a jet flow that is supersonic ($M_{jet} > 1$) and worked for this case. However, if the jet flow would have been subsonic the "Subsonic $p_0 - T_0$ Inflow/Outflow" boundary condition would have been used instead [12].

3.4.2.6 Inviscid, Viscous, and Thermo-Chemical Models

The inviscid and viscous models need to be set up next. The inviscid model uses an upwind-biased third order spatially accurate Roe Flux scheme. To prevent non-physical oscillations from occurring during the calculations, a Van Albada limiter is invoked.

All of the viscous terms were included in the computation, and Mentor's shear stress transport *K-ω* Turbulence model was used. The GASP Manual [12] suggests using a *K-ω* limiting factor in order to add stability to the system of equations during the time integration process. So, the limiting factor was set to 2000 times the viscosity. Wall functions were disabled during the computations, but compressibility corrections were enabled.

It was assumed that the jet-wing uses cold exhaust from the fan of a turbojet engine, so a complex chemical model wasn't necessary even though GASP can model real gas effects including chemical reactions. Therefore, the model for the inboard EET airfoil uses a perfect gas chemistry model with its chemical composition frozen.

3.4.2.7 Run Settings

GASP computed the steady state solution using a Gauss-Seidel implicit time integration scheme. This was done using three different grid sequences as described in Section 3.4.2.2: coarse, medium, and fine. The solution was first run and converged on the coarse grid and then the final result was interpolated to the medium grid as the initial condition. The same was then done to the medium grid, with its solution interpolated to the fine grid as its initial condition. Finally, the solution was run and converged on the fine grid. The overall residual which is the basis for convergence is the sum of the L^2 norms of all of the governing equations for each cell. Convergence normally occurs when the residual has been reduced by 4 to 6 orders of magnitude on each grid. Occasionally, problems arise with convergence due to very rapid decreases in the L^2 norm (11 orders of magnitude in less then 100 iterations for the coarse grid) and so the total forces in the x- and y-directions need to be monitored ($F_{x,total}$ and $F_{y,total}$). Convergence then occurs when there is no appreciable change in both $F_{x,total}$ and $F_{y,total}$, which can be seen in Figure 3.20. The coarse grid was run for 10,000 cycles with a time step of Q_∞, min and max *CFL* values of 1, and uncoupled turbulence. The *CFL* is the Courant number which is used to guarantee convergence. By changing the *CFL* value, one can help the problem converge faster. The medium and fine grids were both split into two runs with a few settings changed. The first medium run had a Q_{local} time step, min and max *CFL* values of 0.5, and again with uncoupled turbulence for 10,000 cycles. The second medium run was set up the same but with the time step changed to Q_∞. Both fine runs were set up with the same settings as the medium runs but the second fine run went longer with 30,000 cycles before convergence for the no jet case and 40,000 cycles for the jet case. The fine grid convergence of the jet case for the inboard EET airfoil can be seen in Figure 3.20. All runs were done on a

SGI Origin 2000 computer which has 32 processors. Typically, these jobs were each run on 8 processors.

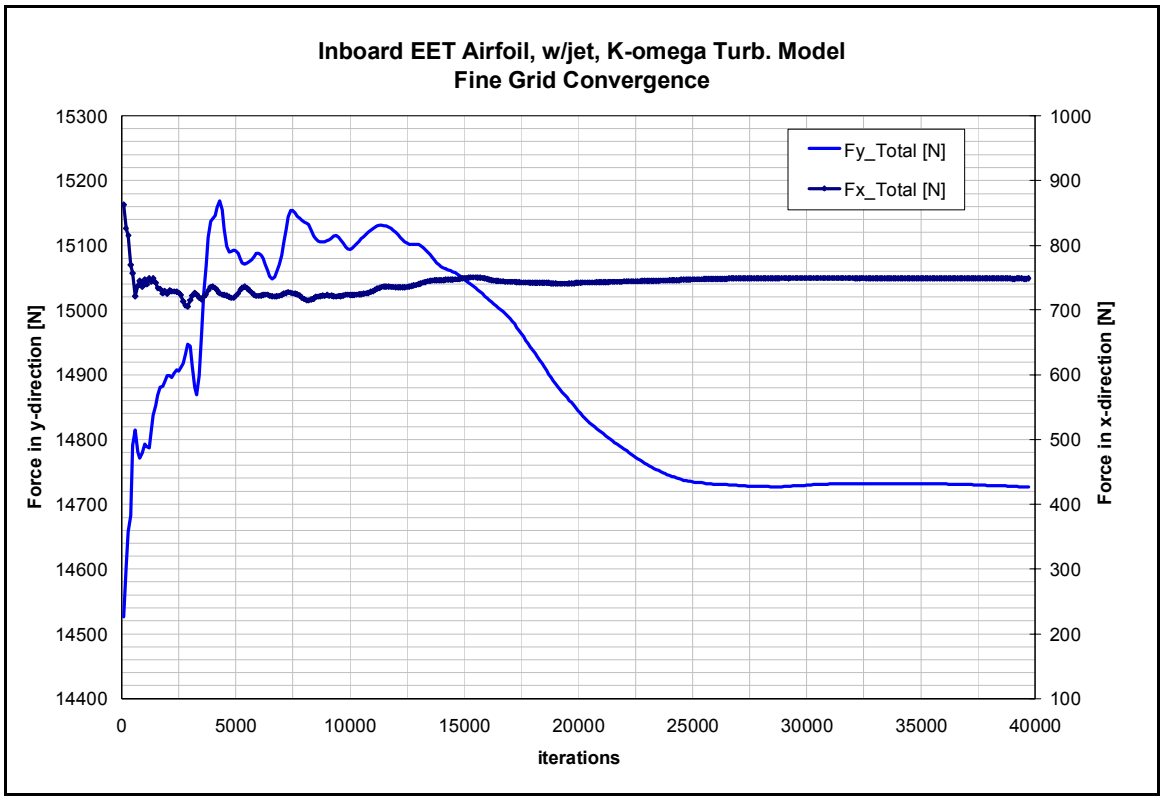

Figure 3.20: Fine Grid Convergence History for the jet case

3.4.2.8 Post Processing

The results from the runs were output by GASP in two different forms: the forces and moments from pressures and shear stresses integrated over the surfaces and the physical properties. The forces and moments were integrated over the airfoil surface and the trailing edge surface (see Figure 3.19) and were output every 100 iterations. The following were included in the output file for each run:

- Fx_Total, Fy_Total: the summation of pressure and viscous shear stress forces in the x- and y-directions
- Fx_Inv, Fy_Inv: the summation of pressure forces in the x- and y-directions

- Fx_Vis, Fy_Vis: the summation of viscous shear stress forces in the x- and y-directions
- $Thrust\_x$, $Thrust\_y$: the summation of the pressure, viscous, and momentum flux forces in the x- and y-directions
- Mz_Total: the moment due to pressure and viscous forces about $\frac{x}{c} = 25\%$
- Mz_Inv: the moment due to pressure forces about $\frac{x}{c} = 25\%$
- Mz_Vis: the moment due to viscous forces about $\frac{x}{c} = 25\%$
- Mz_Thrust: the moment due to pressure, viscous, and momentum flux forces about $\frac{x}{c} = 25\%$

The convergence of the solution could be tracked since the solution was output every 100 iterations. The next section will explain the procedure used to compute the force and moment coefficients. The physical properties of the flowfield were also output every 100 iterations by GASP. The following quantities were included in the output at every point:

- x, y: the grid point coordinates
- M: the Mach number
- u, v: the velocity components
- p, T, ρ, C_p: the pressure, temperature, density, and pressure coefficient
- TKE: the turbulent kinetic energy
- ω: the turbulence frequency

To easily analyze the flowfield data further, the output files were loaded into *Tecplot*. This allowed for the creation of contour and streamline plots. Also, *Tecplot* can easily be used to extract the surface pressure distribution plot and wake profiles.

3.4.3 Force Coefficient Calculations

Before the force coefficients can be calculated, it is first important to understand how the CFD problem is set up in GASP. The airfoil chord line is aligned with the global *x*-axis of the global coordinate system and is oriented horizontally. A velocity vector, U_∞, oriented at an angle α (the angle of attack) is used to apply the freestream flow. When the jet is applied, it exits the trailing edge (TE) with a velocity U_{jet} at an angle τ with respect to the chord line. The lift and drag are aligned with a coordinate system rotated by an angle equal to alpha when calculated. The set-up for this problem can be seen in Figure 3.21.

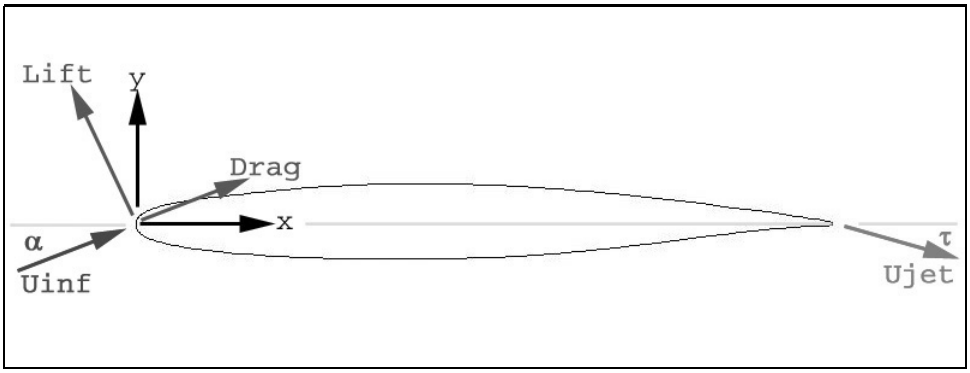

Figure 3.21: Orientation of the jet-wing set up in GASP [15]

As was stated previously, the grid created for this model is a 2 zone C-grid (see Figure 3.15) due to the thick trailing edge. These two zones are the thin area that extends downstream from the trailing edge and the other is the rest of the computational domain. In computing the forces on both of these zones, a notation needed to be established in order to keep the forces from both zones straight. The subscript "TE" was used to denote those forces generated by the blunt trailing edge (such as base drag) and the subscript "surf" was used to denote those forces on the rest of the airfoil surface.

The process used to calculate the force coefficients followed that used by Dippold [15]. This process used four quantities that were output from GASP: *Fx_Total*, *Fy_Total*, *Thrust_x* and *Thrust_y*. These are computed from the pressure and viscous forces integrated over the element faces of the airfoil surface and the

trailing edge. The *x*- and *y*-components of the sum of all the pressure and viscous forces comprise the *Fx_Total* and *Fy_Total* forces. Dippold showed these forces can be written in the following set of equations:

$$\begin{aligned} Fx\_Total &= \sum \left[\left(\vec{F}_{pressure} + \vec{F}_{viscous} \right) \bullet \hat{i} \right] \\ Fy\_Total &= \sum \left[\left(\vec{F}_{pressure} + \vec{F}_{viscous} \right) \bullet \hat{j} \right] \end{aligned} \tag{3.7}$$

The vectors $\hat{i}$ and $\hat{j}$ are unit vectors in the *x*- and *y*-directions, respectively. The *Thrust_x* and *Thrust_y* forces include forces due to momentum flux if there is flow through the surface, as with a jet, as well as the summed pressure and viscous forces.

$$\begin{aligned} Thrust\_x &= \sum \left[\left(\vec{F}_{pressure} + \vec{F}_{viscous} + \vec{F}_{momentumflux} \right) \bullet \hat{i} \right] \\ Thrust\_y &= \sum \left[\left(\vec{F}_{pressure} + \vec{F}_{viscous} + \vec{F}_{momentumflux} \right) \bullet \hat{j} \right] \end{aligned} \tag{3.8}$$

The forces *Thrust_x* and *Thrust_y* are equal to the forces *Fx_Total* and *Fy_Total* in most of the computational domain. According to Dippold [15], where a jet is added is the only place that the forces due to momentum flux appear. In these runs, the jet is added to the trailing edge although it can actually be added to any surface along the airfoil. A force is created at the trailing edge surface by the added mass and momentum from the jet. Therefore, Dippold showed that the thrust from the jet, as given by GASP, can be written as:

$$Thrust_{GASP} = \sqrt{\begin{aligned} &\left[\left(Thrust\_x_{surf} - Fx\_Total_{surf} \right) + \left(Thrust\_x_{TE} - Fx\_Total_{TE} \right) \right]^2 \ldots \\ &+ \left[\left(Thrust\_y_{surf} - Fy\_Total_{surf} \right) + \left(Thrust\_y_{TE} - Fy\_Total_{TE} \right) \right]^2 \end{aligned}} \tag{3.9}$$

This, however, is not the full calculation of the jet thrust. Dippold took a look at the well-known thrust equation for a jet:

$$Thrust_{jet} = \dot{m}_{jet} \cdot \left(U_{jet} - U_{\infty} \right) + \left(p_{jet} - p_{\infty} \right) \cdot \left(b_{jet} \cdot h_{jet} \right) \tag{3.10}$$

In Equation 3.10, the b_{jet} is the span of the jet. This equation shows that the thrust is dependent on the jet velocity, U_{jet}, and the inlet velocity, which is typically the freestream velocity, U_{∞}. In the CFD jet-wing model used by GASP, the thrust is calculated as $\dot{m}_{jet} \cdot U_{jet}$ but with the $\dot{m}_{jet} \cdot U_{\infty}$ term missing, the jet becomes a rocket. So Dippold [15] added this term to the trust calculated by GASP:

$$\begin{aligned} \dot{m}_{jet} \cdot U_\infty &= b_{jet} \cdot h_{jet} \cdot \rho_{jet} \cdot U_{jet} \cdot U_\infty \\ Thrust_{jet} &= Thrust_{GASP} - b_{jet} \cdot h_{jet} \cdot \rho_{jet} \cdot U_{jet} \cdot U_\infty \end{aligned} \tag{3.11}$$

Again, following the process used by Dippold, two sets of forces were calculated: forces due to the airfoil alone, without the jet and forces due to the airfoil and the jet. Equation (3.12) shows the lift and drag forces from the airfoil alone.

$$\begin{aligned} L &= -\left(Fx\_Total_{surf} + Fx\_Total_{TE}\right) \cdot \sin(\alpha) + \left(Fy\_Total_{surf} + Fy\_Total_{TE}\right) \cdot \cos(\alpha) \\ D &= \left(Fx\_Total_{surf} + Fx\_Total_{TE}\right) \cdot \cos(\alpha) + \left(Fy\_Total_{surf} + Fy\_Total_{TE}\right) \cdot \sin(\alpha) \end{aligned} \tag{3.12}$$

The respective coefficients can then be calculated as follows:

$$\begin{aligned} C_L &= \frac{L}{\frac{1}{2} \cdot \rho_\infty \cdot U_\infty^2 \cdot c \cdot b} \\ C_D &= \frac{D}{\frac{1}{2} \cdot \rho_\infty \cdot U_\infty^2 \cdot c \cdot b} \end{aligned} \tag{3.13}$$

The value of c in this equation is the reference chord length of the airfoil used in creating the grid and in GASP. The net lift and drag forces from the airfoil and the jet can be seen in equation (3.14).

$$\begin{aligned} L_{Net} &= -\left(Thrust\_x_{surf} + Thrust\_x_{TE}\right) \cdot \sin(\alpha) + \left(Thrust\_y_{surf} + Thrust\_y_{TE}\right) \cdot \cos(\alpha) \ldots \\ &\quad + \left(b_{jet} \cdot h_{jet} \cdot \rho_{jet} \cdot U_{jet} \cdot U_\infty\right) \cdot \sin(\alpha + \tau) \\ D_{Net} &= \left(Thrust\_x_{surf} + Thrust\_x_{TE}\right) \cdot \cos(\alpha) + \left(Thrust\_y_{surf} + Thrust\_y_{TE}\right) \cdot \sin(\alpha) \ldots \\ &\quad + \left(b_{jet} \cdot h_{jet} \cdot \rho_{jet} \cdot U_{jet} \cdot U_\infty\right) \cdot \cos(\alpha + \tau) \end{aligned} \tag{3.14}$$

Positive thrust into the freestream flow is indicated by a negative D_{Net} term. For the jet-wing to be self-propelled, the D_{Net} term needs to equal zero. It can be noted that in equation (3.14), the $b_{jet} \cdot h_{jet} \cdot \rho_{jet} \cdot U_{jet} \cdot U_\infty$ term was included to give the correct thrust. Finally, the force coefficients for the net lift and drag can be computed from:

$$\begin{aligned} C_{L_{Net}} &= \frac{L_{Net}}{\frac{1}{2} \cdot \rho_\infty \cdot U_\infty^2 \cdot c \cdot b} \\ C_{D_{Net}} &= \frac{D_{Net}}{\frac{1}{2} \cdot \rho_\infty \cdot U_\infty^2 \cdot c \cdot b} \end{aligned} \tag{3.15}$$

3.4.4 Jet Coefficient Calculations

One of the things looked at during this study is the effect of the jet-wing on the flowfield when deflected like a flap. This basically is the idea of a jet flap which as stated previously is usually used in high lift applications with large jet deflection angles and high thrust, whereas the jet-wing is used during cruise conditions. One of the main features of this study is looking at the jet coefficient, C_J, which can be calculated using Equation (3.16). For a self-propelled jet-wing, when the thrust exactly cancels out the drag, the jet coefficient C_J will simply be equal to the local drag coefficient, $C_{D_{local}}$, shown in Equation (3.17).

$$C_J = \frac{m \cdot U_{jet}}{\frac{1}{2} \cdot \rho \cdot U_\infty^2 \cdot S} = \frac{T}{q \cdot S} \tag{3.16}$$

$$C_J = \frac{D_{local}}{q \cdot S} = C_{D_{local}} \tag{3.17}$$

Following the steps taken by Dippold [15], the MSES results chosen for the jet-wing calculations gives a lift coefficient of $C_L = 0.6584$ with a corresponding drag coefficient of $C_{D_{local}} = 0.0085$. This means that for a self-propelled jet, the Inboard EET airfoil need a jet coefficient of $C_J = 0.0085$. Dippold found that when the jet coefficient is much less than 1.0, then there is no significant effect on either the lift or the pressure distribution from the jet-wing.

3.5 Jet-wing Distributed Propulsion Results

The first results obtained for inboard EET airfoil were from the no-jet case. After these results were obtained, the resultant drag coefficient, $C_D = 0.0118$, and the pressure at the trailing edge, $p_{TE} = 23909 \, {}^{\mathrm{N}}/_{\mathrm{m}^2}$, were used to calculate the jet Mach Number, $M_{jet} = 1.059$, and density, $\rho_{jet} = 0.3806 \, {}^{\mathrm{kg}}/_{\mathrm{m}^3}$, that were needed for the jet to be self propelled. The propulsive efficiency for the inboard EET airfoil was found using equation 3.18 to be $\eta_P = 81.0\%$.

$$\eta_P = \frac{2}{1 + \frac{U_{jet}}{U_\infty}} \tag{3.18}$$

The net lift coefficient for the jet case was found to be lower than the net lift coefficient for the jet-wing case. It would be necessary to increase the angle of attack for the jet-wing case in order to match lift coefficients. A comparison of the pressure distribution from GASP and MSES for the No Jet Case can be seen in Figure 3.22. These runs were both obtained with the same angle of attack, $\alpha = 0.521°$. It can be seen that the comparison is fairly good for both programs. The bottom surface pressures are almost exactly the same. The main difference in the two pressure distributions occurs at the shock location. MSES predicts the shock to be about 10% further downstream than GASP, which would explain the difference in lift coefficients. Another MSES run was made in order to mach lift coefficients. Figure 3.23 shows the pressure distribution comparison for the matched C_L values. This comparison is much better between MSES and GASP, with only very minor differences.

Figure 3.24 shows the pressure distribution for both the No-Jet and Jet cases for the inboard EET airfoil, and Table 3.8 shows the force coefficients for both cases. The pressure distribution shows the difference in C_L. The bottom surface pressures appear to be very similar but the pressures along the top surface of the airfoil differ much more for different lift coefficients. There is a small difference in the location of the upper surface shock for both the Jet and No-Jet cases. The pressures on the upper surface of the Jet Case are larger than the pressures on the upper surface of the No-Jet Case, giving more lift to the No-Jet Case. One would expect the pressure distributions to be almost exactly the same for both cases if the net lift coefficient values were the same.

Figure 3.25 shows the downstream velocity profile for the jet and no jet cases. Here it can be seen that by adding the jet, the wake is partially filled in which explains the increased propulsive efficiency. The profiles for the two cases

are not better aligned due to the difference in circulation, which is due to the difference in the C_L values between the cases.

The streamlines and Mach contours for the No-Jet Case can be seen in Figure 3.26 and Figure 3.27. These plots show clearly the shock on the upper surface at about 25% of the chord that was seen in the pressure distribution. There also appears to be another shock near the leading edge of the airfoil. There was no separation anywhere along the airfoil, but there is some recirculation around the blunt trailing edge of the airfoil. This recirculation is the formation of vortices near the trailing edge base of the inboard EET airfoil.

Figure 3.28 and Figure 3.29 show the streamlines and Mach contours for the Jet Case. The streamlines for the Jet Case appear very similar to the No-Jet Case for most of the flowfield around the airfoil. A shock can be seen on the top of the airfoil and also a small shock near the leading edge. The main differences between the flow fields occur at the trailing edge. The jet can be seen exiting the trailing edge of the airfoil filling in the flow and pulling the streamlines to blend smoothly with the jet. The jet removed the vortices from the trailing edge base of the airfoil that were seen in the No-Jet Case.

Figure 3.30 and Figure 3.31 show the pressure contours around the EET inboard airfoil. Looking closely near the trailing edge, it can be seen that there are a few weak shocks present in the jet. This tells us that there may need to be a few iterations to better match the pressure of the jet with that of the flow at the trailing edge of the airfoil. Even with this small difference in pressures near the trailing edge base, adding the jet to the inboard EET airfoil simplified the flow and helped to increase the propulsive efficiency. This shows that in this case adding something to the flow actually simplifies the flowfield.

This inboard EET airfoil started out with a thick trailing edge, 0.66% of the chord, to begin with. Therefore, it was not necessary to double the trailing edge thickness in order to increase the propulsive efficiency. This is fortunate for this case, because Dippold [15] learned that increasing the trailing edge thickness also

increases the drag on the airfoil. This is an unwanted effect. So, these inboard EET airfoil results showed that it was indeed a good candidate for the jet-wing.

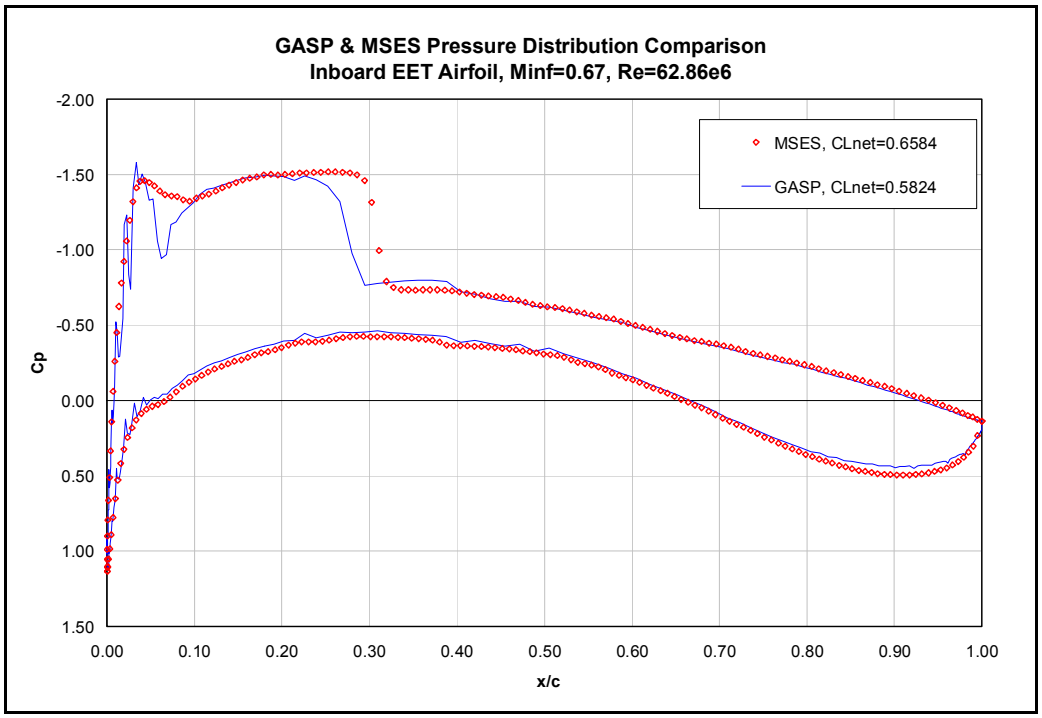

Figure 3.22: GASP and MSES Pressure Distribution Comparison for the No Jet Case

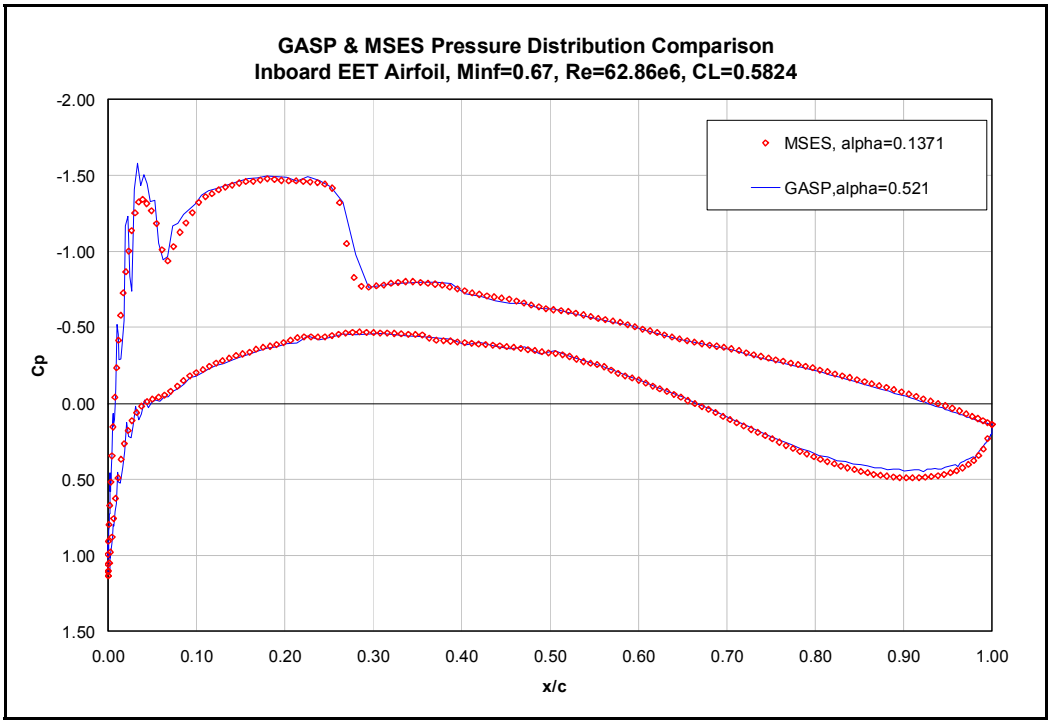

Figure 3.23: GASP and MSES pressure distribution comparison for matching CL

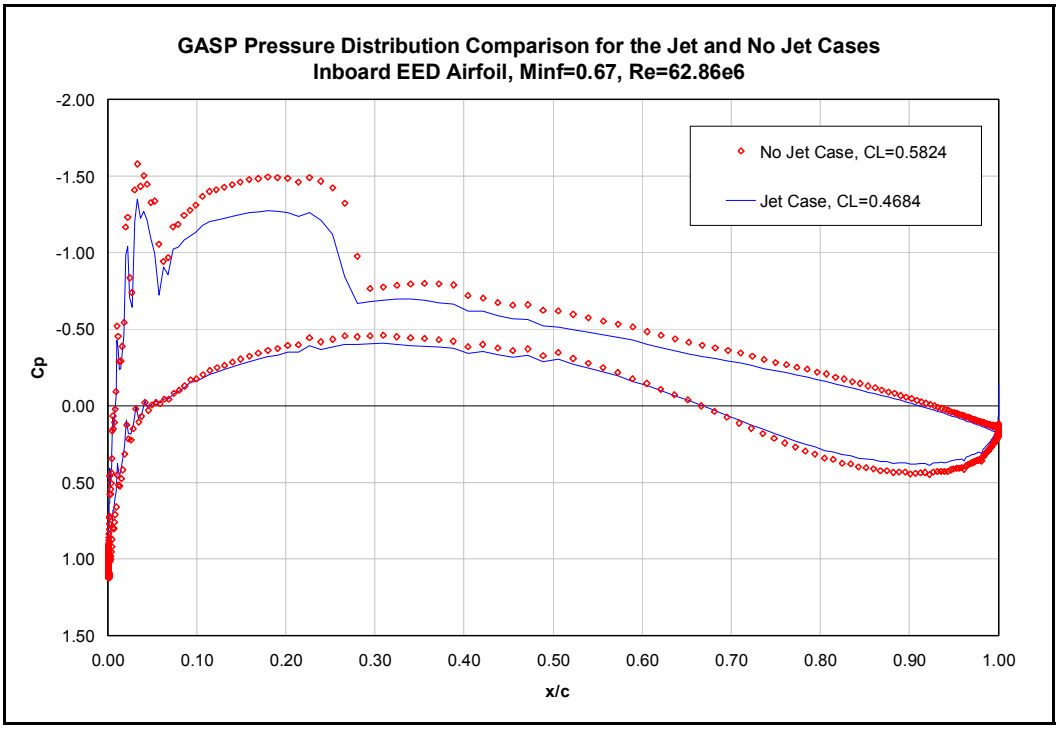

Figure 3.24: GASP pressure distribution comparison for the Jet and No Jet Cases

Airfoil	Inboard No Jet	Inboard w/ Jet
Alpha [deg]	0.521	0.521
Tau [deg]	0.000	3.000
M_{jet}	0.000	1.059
Prop. Efficiency	0.00%	81.00%
C_L	0.5824	0.4684
C_D	0.0118	0.0098
Net C_L	0.5824	0.4684
Net C_D	0.0118	0.0008
C_J	0.0000	0.0089

Table 3.8: Force Comparison for the Jet and No Jet Cases

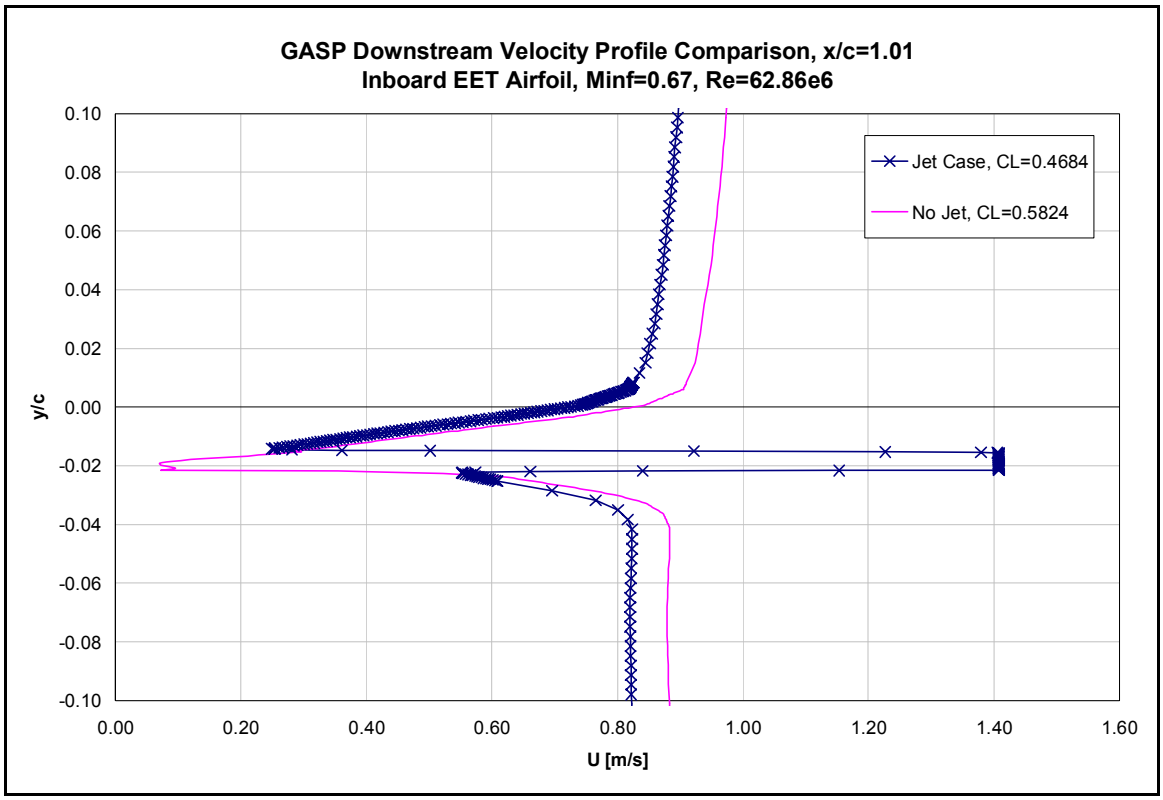

Figure 3.25: Downstream velocity profile comparison

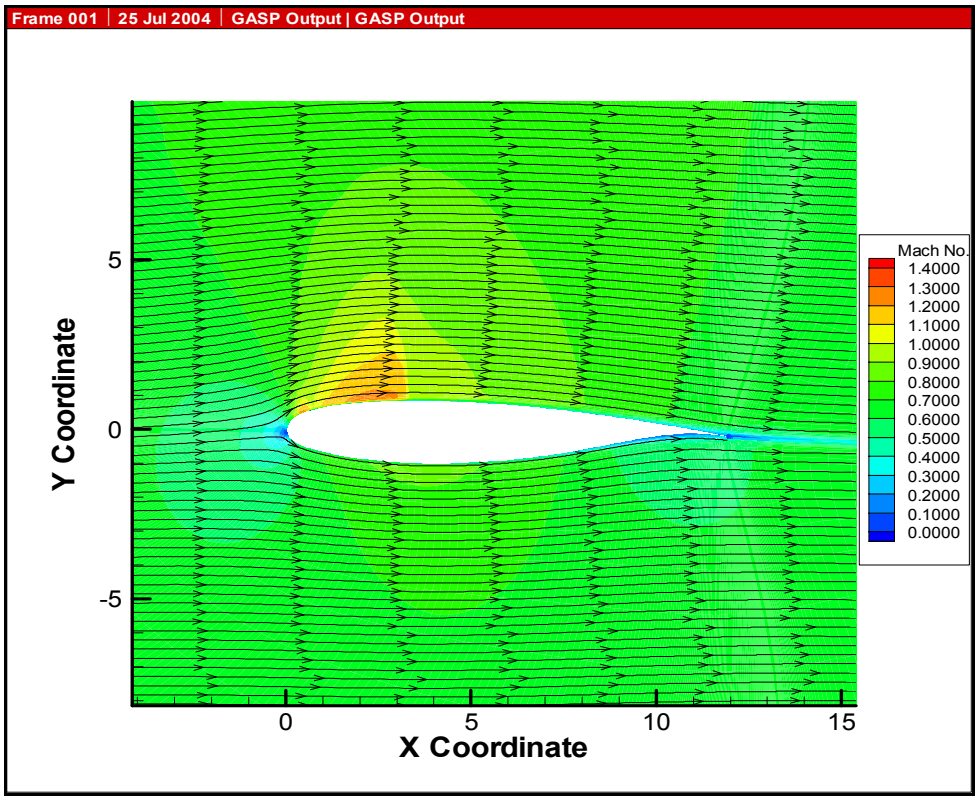

Figure 3.26: Streamlines and Mach Contours for the No Jet Case

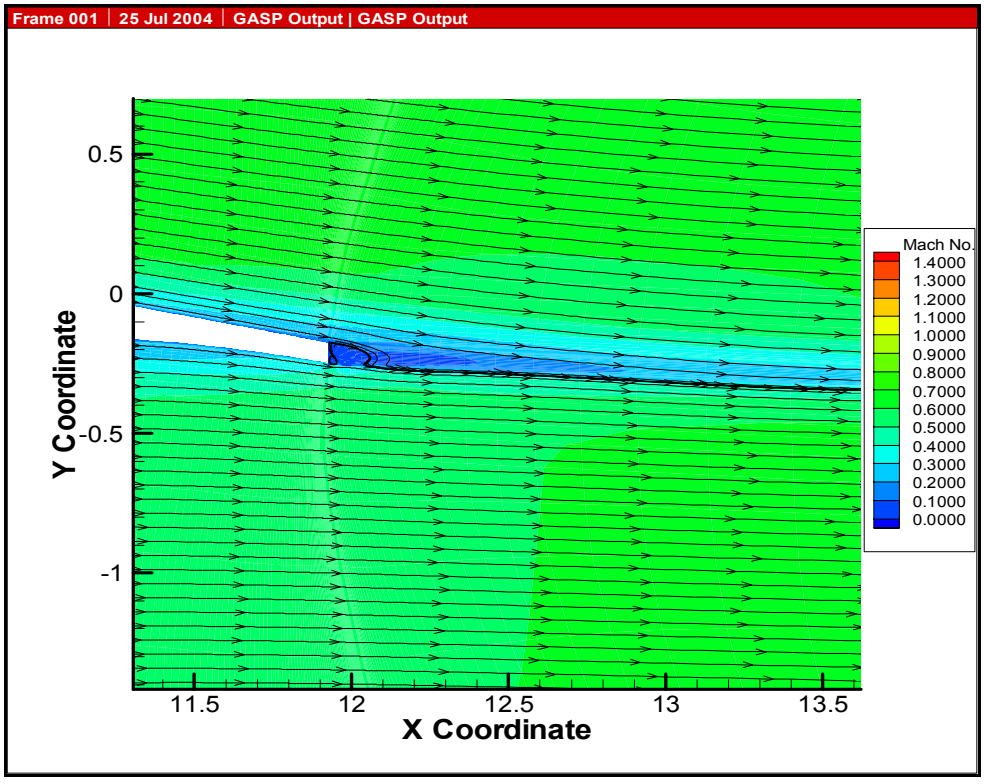

Figure 3.27: Streamlines and Mach contours near the trailing edge for No Jet Case

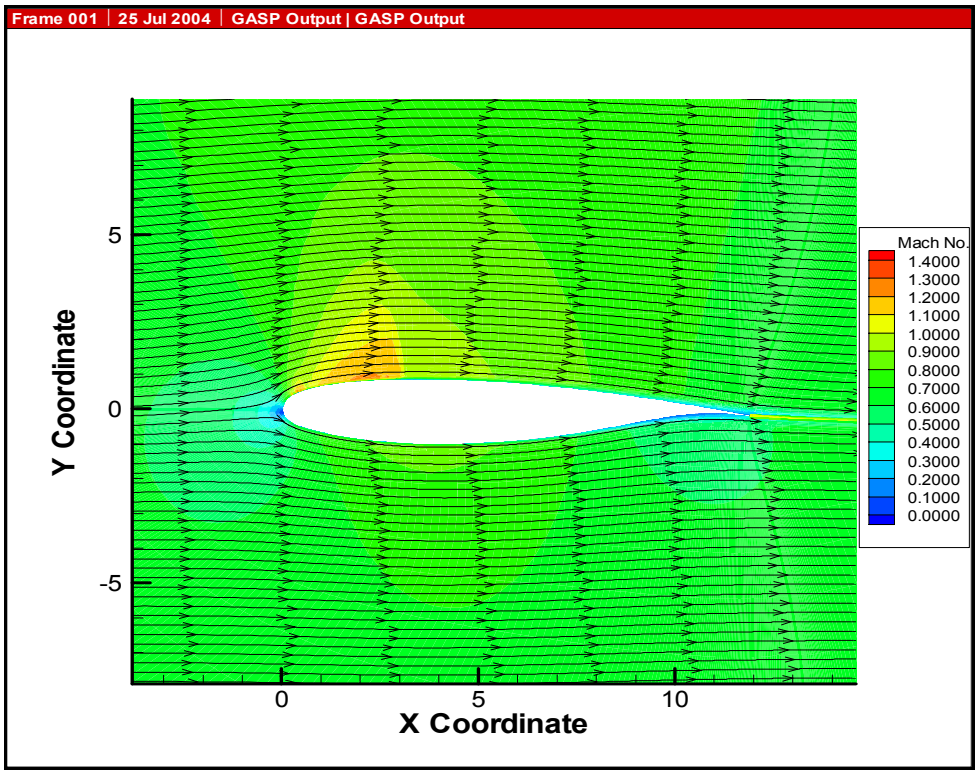

Figure 3.28: Streamlines and Mach contours for the Jet Case

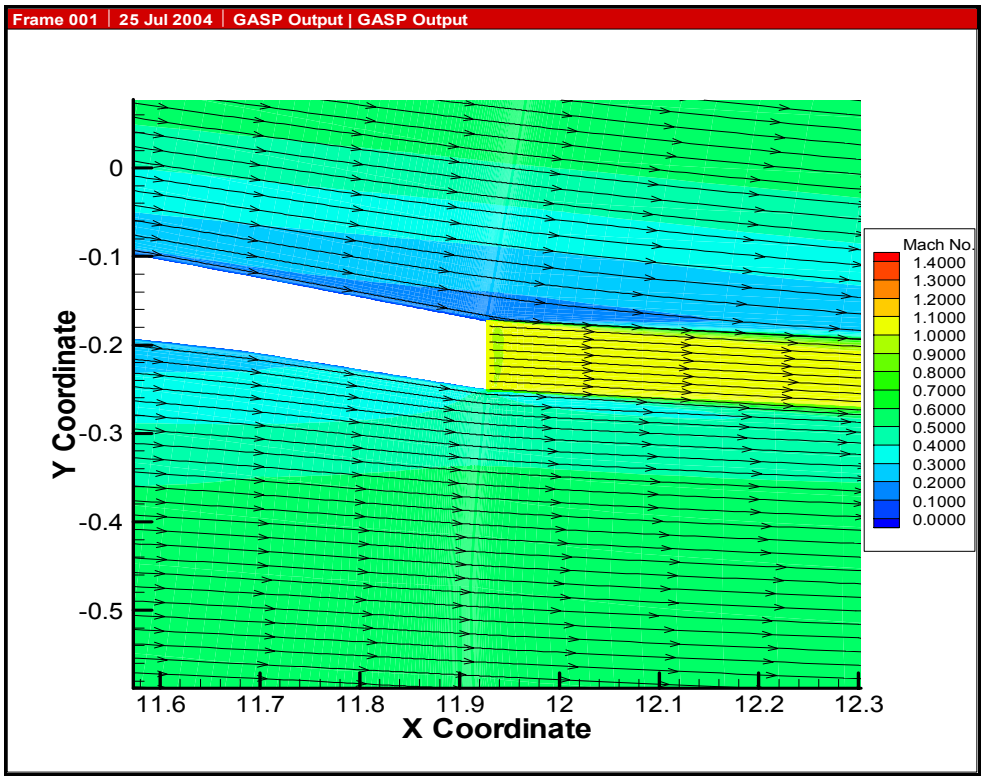

Figure 3.29: Streamlines and Mach contours near the trailing edge for the Jet Case

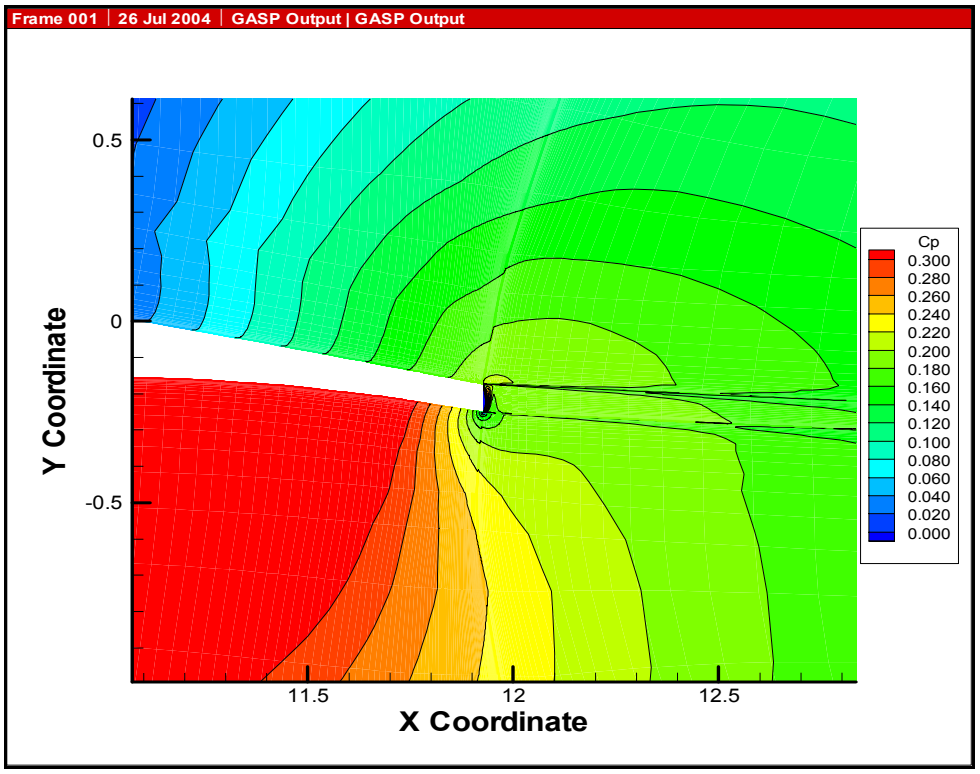

Figure 3.30: Pressure contours for the No Jet Case

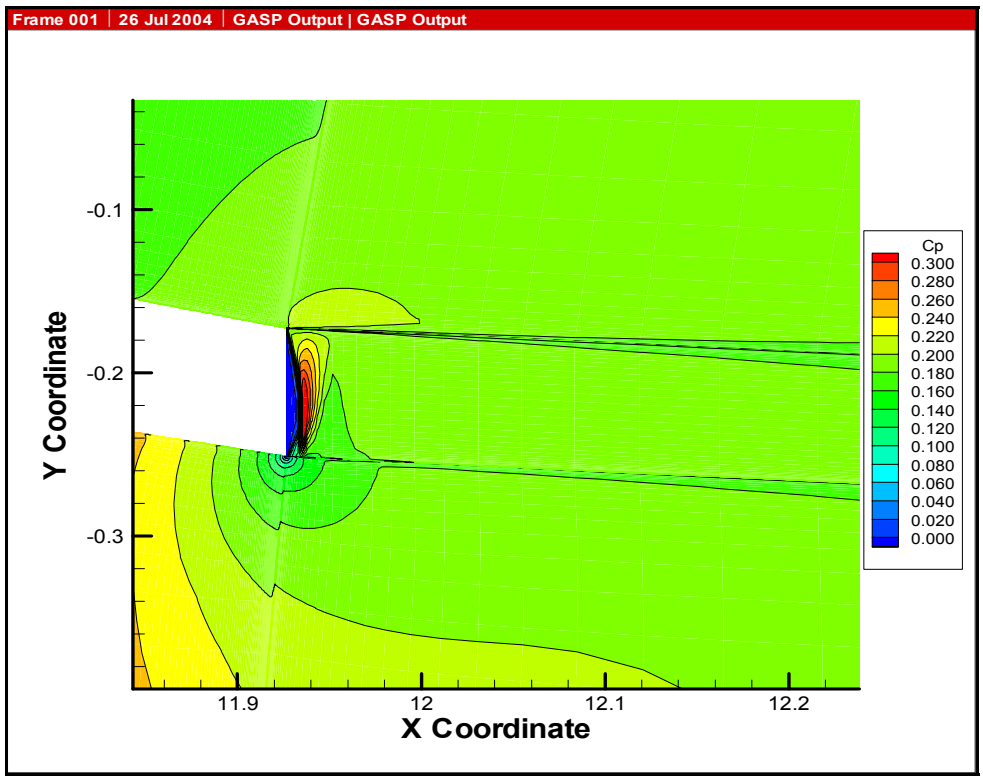

Figure 3.31: Close up of pressure contours in jet region for the Jet Case

Chapter 4: Trailing Edge Noise

4.1 Simplified Noise Approach

The other main purpose of this task was to create a simplified boundary layer approach to calculating the trailing edge noise metric and to compare these results with a previously documented computationally expensive RANS noise study done by Hosder et al [20]. The approach was to use the Boundary Layer Applets [10], Java codes that solve boundary layer problems, to obtain the information needed to calculate the characteristic turbulence length scale, l_0, and the characteristic turbulence velocity, u_0. These codes will give boundary layer characteristics that include: boundary layer height, δ, displacement thickness, δ^*, momentum thickness, θ, and the skin friction coefficient, C_f.

The first step in the simplified noise approach was deciding where in the boundary layer the maximum TKE would occur at the trailing edge of a wing. The eddy viscosity concept was used to model the TKE as shown in equation (4.1) [11]:

$$\mu_T = \rho \cdot \sqrt{TKE} \cdot l_t \tag{4.1}$$

where μ_T is the eddy viscosity and l_t is the turbulent length scale. Following boundary layer theory it can be said that the maximum eddy viscosity occurs at the junction of the log region and outer region and the same is true for the turbulent length scale. Equation (4.2) shows equations used for both the eddy viscosity and the turbulent length scale in the log region.

$$\begin{aligned} \mu_{T,\log} &= \kappa \cdot \rho \cdot u_* \cdot y \\ l_t &= C_{Dw}^{1/4} \cdot \kappa \cdot y \end{aligned} \tag{4.2}$$

where κ is a constant taken to be 0.41, C_{Dw} is also a constant taken to be 0.09, and u_* is the friction velocity. Substituting equation (4.2) into equation (4.1), a simplified equation can be found for the TKE:

$$\sqrt{TKE} = \frac{u_*}{C_{Dw}^{1/4}} \tag{4.3}$$

This equation shows that the TKE is constant in the log region of the boundary layer. The decision was then made that the turbulence length scale and the turbulence velocity would be calculated at the junction of the log and outer regions of the boundary layer.

The eddy viscosity was used to determine the location for each case where the junction of the log and outer regions occurred. Equation (4.2) shows the definition of the eddy viscosity in the log region and equation (4.4) shows the definition of the eddy viscosity in the outer region.

$$\mu_{T,O} = \kappa \cdot \rho \cdot U_e \cdot \delta^* \tag{4.4}$$

where U_e is velocity at the edge of the boundary layer. Setting $\mu_{T,O} = \mu_{T,\log}$ we find that the location of the junction of the log and outer regions occurs at:

$$\frac{y}{\delta} = \left(\frac{0.018}{\kappa}\right)\frac{U_e}{u_*} \tag{4.5}$$

The friction velocity can be written in terms of the skin friction coefficient as seen in equation (4.6) [11]. Using this and then simplifying equation (4.5) a more useful form of the junction can be obtained.

$$\frac{u_*}{U_e} = \sqrt{\frac{\tau_w}{\rho U_e^{\,2}}} = \sqrt{\frac{C_f}{2}} \tag{4.6}$$

$$y = \left(\frac{0.018 \cdot \delta}{\kappa}\right)\sqrt{\frac{2}{C_f}} \tag{4.7}$$

The location in the boundary layer where the junction occurs, shown in equation (4.7), is then used to calculate the turbulent length scale at this location from equation (4.2). Finally, the turbulent velocity can be calculated from the constant TKE (see equation (4.3)) value found in the log region:

$$u_0 = \sqrt{TKE} \tag{4.8}$$

4.2 *Representative Wing Section*

One of the main objectives of this part of this research project is to compare our simplified approach of calculating the trailing edge noise metric with those results obtained through the more computationally expensive CFD calculations made by Hosder et all [20]. So the choice of the representative wing section followed the choice of airfoil data used in that study. The supercritical airfoil: SC(2)-0714 was used in that study and so will also be used here. Figure 4.1 shows this airfoil section.

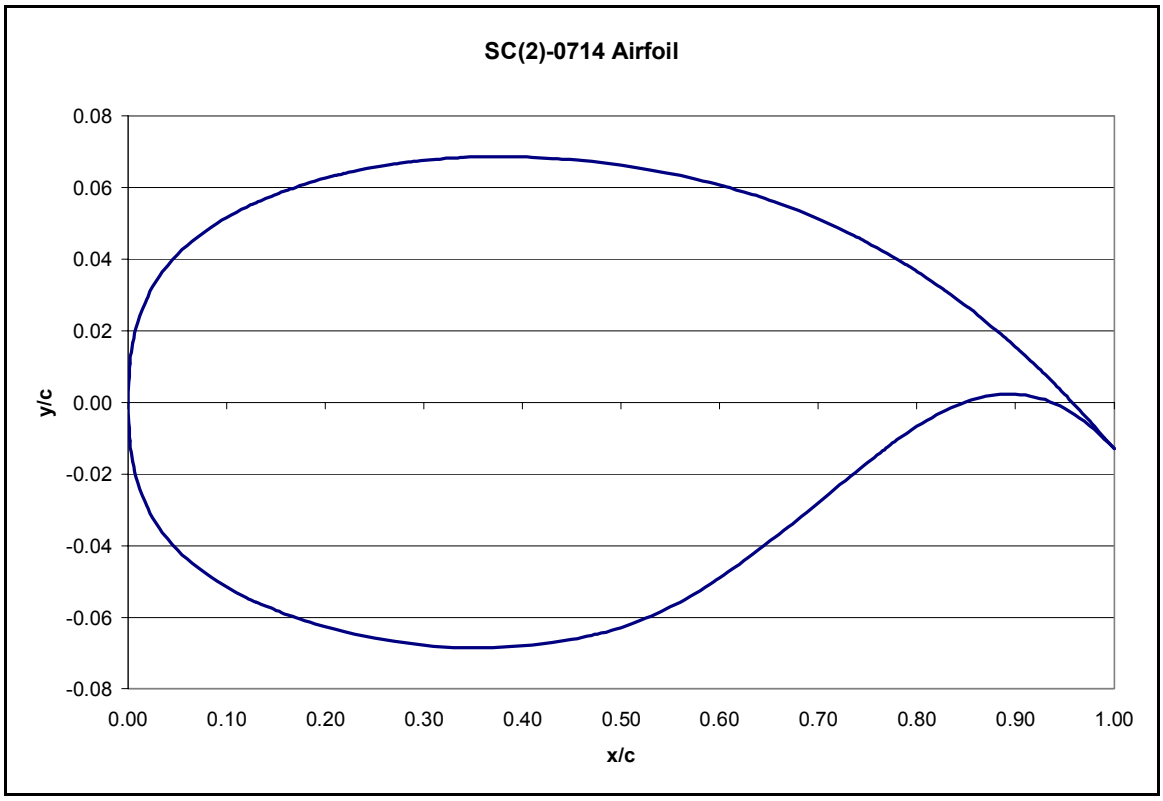

Figure 4.1: Supercritical airfoil with 14% thickness to chord ratio.

The calculations made on this airfoil were performed at the same freestream conditions for a number of different cases. The chord length for the airfoil was taken to be 9.54 m with a freestream velocity of 67.94 m/s. Table 4.1 shows the freestream data used for all cases run on the airfoil. The only thing

that changed for each case was the angle of attack, α, and hence the lift coefficient, C_L. Table 4.2 shows the data for each case run.

U_∞	67.94 m/s
c	9.54 m/s
Re_c	4.40E+07
μ_∞	1.78E-05 kg/m-s
a_∞	339.7 m/s
ρ_∞	1.2115 kg/m^3

Table 4.1: Freestream properties for supercritical airfoil runs

CASE	α(deg)	C_L
1	0.00	0.550
2	2.00	0.788
3	6.00	1.245
4	8.00	1.461
5	10.00	1.665
6	12.00	1.853
7	14.00	2.020
8	16.00	2.159

Table 4.2: Run data for supercritical airfoils

4.3 Boundary Layer Applets

The Java Applets [10] were developed at Virginia Tech as a way for engineering students to enhance their education. Many engineering tools were coded and put on the internet for students to use. This research project uses these applets to obtain the boundary layer data needed to estimate the trailing edge noise metric of an airfoil. These applets are much less computationally expensive than the full RANS CFD runs used by Hosder et all [20]. The RANS CFD runs takes days compared to only minutes to run the applets. The first step in using these codes is to obtain the surface pressure distribution in the form of the ratio of the local edge velocity to the freestream velocity, $\frac{U_e}{U_\infty}$.

To obtain the surface pressure distribution, the Vortex Panel Method Java code was used. The vortex panel method is a method that computes the

aerodynamics of airfoil sections in ideal flows where the effects of compressibility and viscosity are negligible. The flow past an airfoil is modeled as the summation of uniform flow and a series of vortex 'panels', or 'sheets', which is arranged in a closed polygon that approximates the actual shape of the airfoil, see Figure 4.2 [10]. The airfoil coordinates are input into the program and then the surface pressure distribution is output.

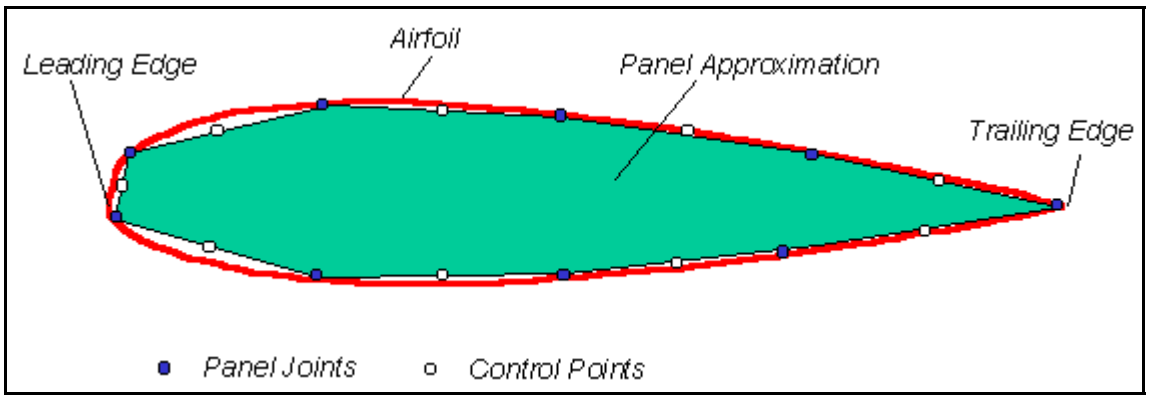

Figure 4.2: Vortex panel approximation of an airfoil. [10]

Once the surface pressure distribution is obtained, the next step is to begin analyzing the airfoil. The analysis begins by entering the pressure distribution along with flow properties and the computational step sizes into the Virginia Tech Boundary Layer Applet *Walz*. The *Walz* code is an integral laminar boundary layer code that is based on the Thwaites-Walz method. Transition from laminar to turbulent flow can be predicted by *Walz* using Michel's method. Next, the *ITBL* code can be run from the "point" of transition using the solution from *Walz*. *ITBL* is a numerical, incompressible turbulent boundary layer code that can use different turbulence models, including the mixing length, eddy viscosity, and TKE models. At first, the *ITBL* code was run with the mixing length model, and then, since the study involves TKE, it was run with the TKE model. Table 4.3 shows the parameters for the supercritical airfoil that are common to all cases.

	WALZ	*ITBL*	*ITBL*
Kinematic viscosity, ν	**1.470e-5 m²/s**	**1.470e-5 m²/s**	**1.470e-5 m²/s**
Freestream velocity, U_∞	**67.94 m/s**	**67.94 m/s**	**67.94 m/s**
Reference length, L	**9.54 m**	**9.54 m**	**9.54 m**
Surface type	**2D body, rounded leading edge**	**--**	**--**
Pressure gradient	**specified**	**specified**	**specified**
Maximum $\frac{x}{L}$	**1.000**	**1.000**	**1.000**
Number of x-steps	**501**	**varies**	**varies**
Turbulence model	**--**	**Mixing Length**	**TKE**
Initial velocity profile	**--**	**Coles Profile**	**Coles Profile**

Table 4.3: Virginia Tech Boundary Layer applet parameters common to all supercritical airfoil cases

In the process of analyzing this supercritical airfoil, the *Walz* code predicted separation before transition could occur in some cases. Therefore, transition had to be forced in those cases by lowering the transition Reynolds number, Re_{trans}. Also as the angle of attack changed, the boundary layer thickness at transition changed as well. So each case, therefore, would have a different number of x-steps and y-steps as well as different step sizes. In each case, the initial x-step size, Δx, was taken to be the initial boundary layer thickness. Then, the chord length was divided by the boundary layer thickness at transition to obtain the number of x-steps. The y-step size, Δy, was calculated by putting 1000 points across the initial boundary layer thickness. The usual way to calculate the number of y-steps was to obtain an estimate of the ending boundary layer thickness and insure that the number of y-steps times Δy was greater than this estimate. This insures that the whole boundary layer is covered. However, no estimate of the ending boundary layer thicknesses could be found. So to insure that the entire boundary layer was covered, the cases were run with an increasing number of y-steps until the ending boundary layer thickness no longer changed. Table 4.4 shows the rest of the input for the 14% thick supercritical airfoil.

	Walz	*ITBL*				
CASE	Flat-plate transition Reynolds number, Re_{trans}	Number of x-steps	Starting $\frac{x}{L}$	Initial boundary layer thickness, δ_{ini}	y-step size	Number of y-steps
1	250,000	8,000	0.0627	0.001229	1.229E-06	800,000
2	250,000	9,000	0.0633	0.001120	1.120E-06	800,000
3	250,000	9,200	0.0723	0.001042	1.042E-06	800,000
4	250,000	9,400	0.0804	0.001029	1.029E-06	800,000
5	25,000	13,000	0.0008	0.000750	7.495E-07	800,000
6	25,000	13,000	0.0975	0.000738	7.377E-07	800,000
7	2,500	17,000	0.1073	0.000563	5.632E-07	800,000
8	2,500	16,000	0.1261	0.000609	6.087E-07	800,000

Table 4.4: Parameters for the 14% thick supercritical airfoil runs.

4.4 Simplified Noise Metric Method Results

There are two different sets of results for each case of the supercritical airfoil runs using the simplified noise metric approach. Each case was run once using the mixing length model and once with the TKE model in the *ITBL* program. The run with the TKE model used an updated version of the code where the TKE profile was among the results printed out. The results from the mixing length model were computed using the method described in Section 4.1, where $\mu_{T,O}$, the eddy viscosity in the outer region of the boundary layer, was set equal to $\mu_{T,\log}$, the eddy viscosity in the log region. However, the results from the TKE model, where the code actually printed out, the TKE profile the results were computed differently. For this set of results, the TKE profiles were plotted, as seen in Figure 4.3, and a maximum TKE value was found. Using this max TKE value, the characteristic turbulent velocity could be calculated using Equation (4.8). As for the characteristic turbulent length scale, this was calculated depending on where the max TKE was located in the boundary layer. When the max TKE was located in the log region of the boundary layer, the turbulent length scale was calculated using equation (4.2) and when the maximum TKE was found in the outer region of the boundary layer, which was

the result in most cases, the turbulent length scale was calculated by the following equation:

$$l_t = 0.09 \cdot \delta \cdot C_{Dw}^{1/4} \tag{4.9}$$

where δ is the boundary layer thickness.

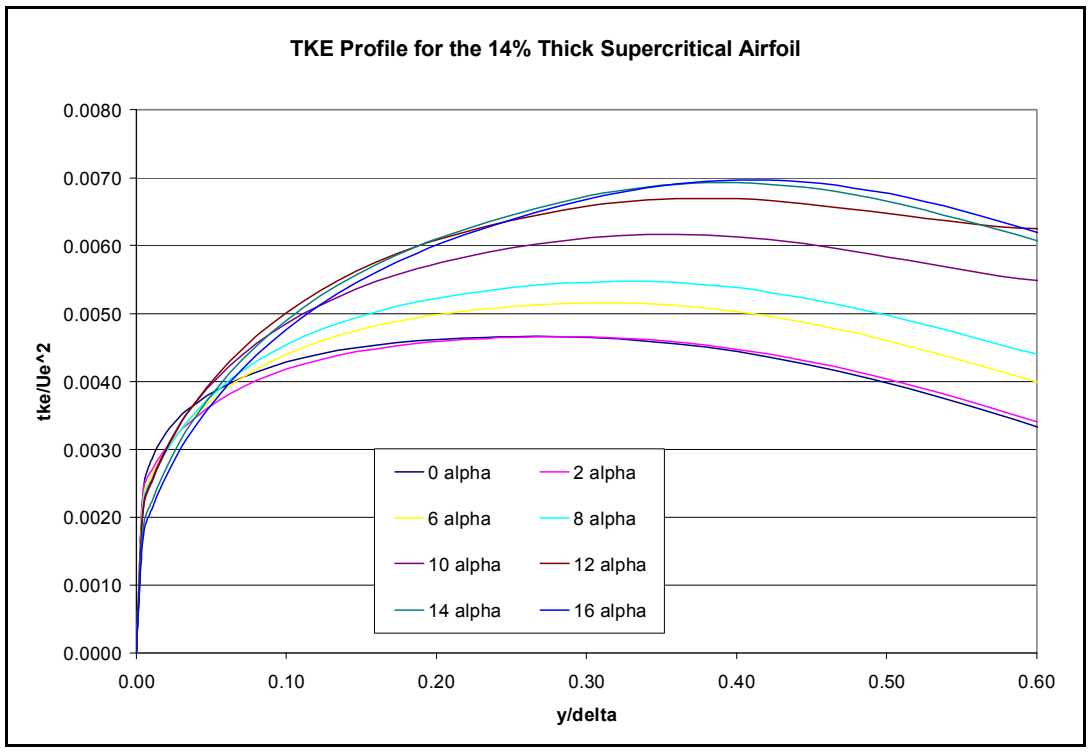

Figure 4.3: TKE Profile for the SC(2)-0714 Airfoil

The results for the 14% thick supercritical airfoil were studied in depth. Figure 4.4 shows the turbulent length scale variation with lift coefficient, C_L, and Figure 4.5 shows the turbulent velocity variation. These graphs show the results as obtained from GASP by Hosder et al [20] as well as the results from the mixing length model and the TKE model runs. For the turbulent length scale, the Boundary Layer Applets [10] give fairly good results for low lift coefficients, but the accuracy is lessened as the lift coefficient is increased. The trend of the results is basically the same for all methods used to predict the turbulent length scale. There was some difference in the results obtained by using the method used with the mixing length model and the results from using the actual max

TKE values but not a significant difference. This gives some credence to the choices made in using this method to predict the characteristic length scale. The turbulent velocity results show similar differences. The results compare fairly well at lower lift coefficient values with larger differences at higher C_L values. It can also be seen that the values obtained from the maximum TKE results show better accuracy than the other Boundary Layer Applet results. This shows that using the actual maximum TKE value is the better way to calculate the characteristic turbulent velocity.

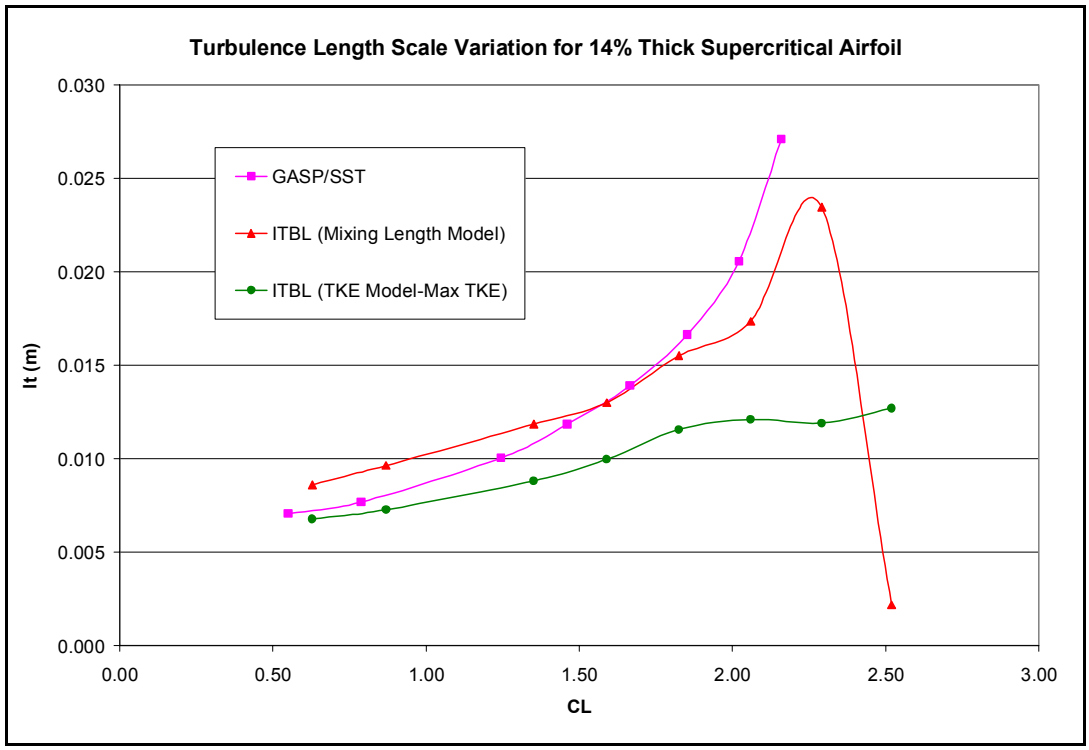

Figure 4.4: Characteristic turbulent length scale results for the 14% thick supercritical airfoil

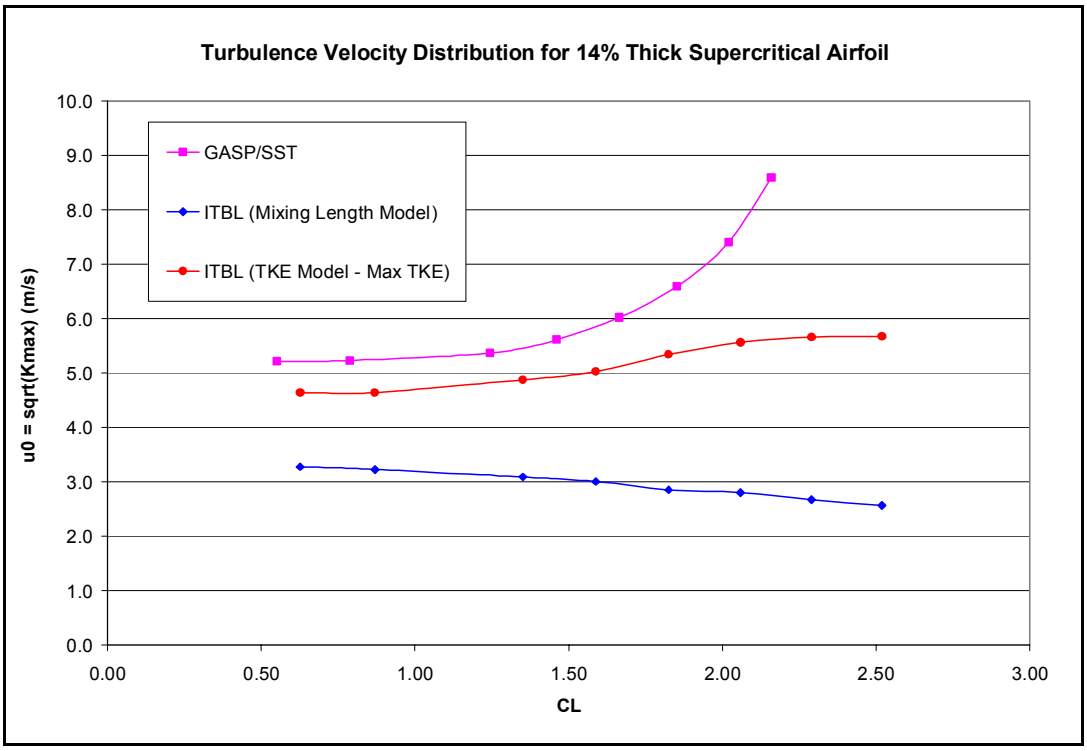

Figure 4.5: Characteristic turbulent velocity results for the 14% thick supercritical airfoil

After looking at the results found from using the Boundary Layer Applets and noticing the differences from GASP, it was decided to compare the trailing edge skin friction coefficients, C_f, and also some pressure data from the GASP with the results obtained from the Java Codes. Figure 4.6 shows the comparison of the trailing edge C_f values for each of the methods used by the Boundary Layer Applets and the GASP results. The results from the Boundary Layer Applets appear to be very similar for both the mixing length model and the TKE model. However, these results appear to be two times larger than the GASP results even though the trend is the same. Figure 4.7 through Figure 4.9 show a few pressure distribution comparisons for the SC(2)-0714 airfoil. For the most part, the pressure distributions compare very well with little differences, except near the trailing edge, where the interests for this project lie. The Vortex Panel Method (VPM) seems to not predict the pressures at the trailing edge of the airfoil very accurately. These differences in the trailing edge pressures gives way

to the differences in the trailing edge skin friction values. This sheds some light on the reasons for the differences between the Boundary Layer Applets and the GASP results. If a better method of calculating the upper surface pressure distribution could be found, this method may provide more accurate results which closer match the results obtained from GASP.

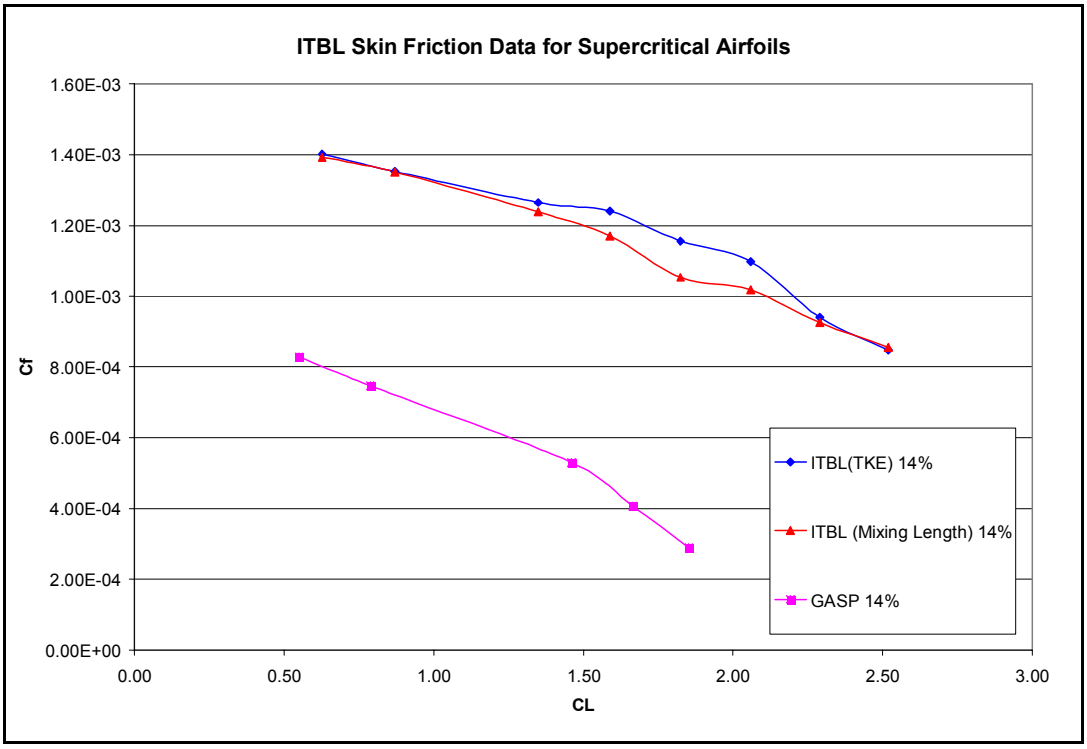

Figure 4.6: Skin Friction Comparison between GASP and the Boundary Layer Applets

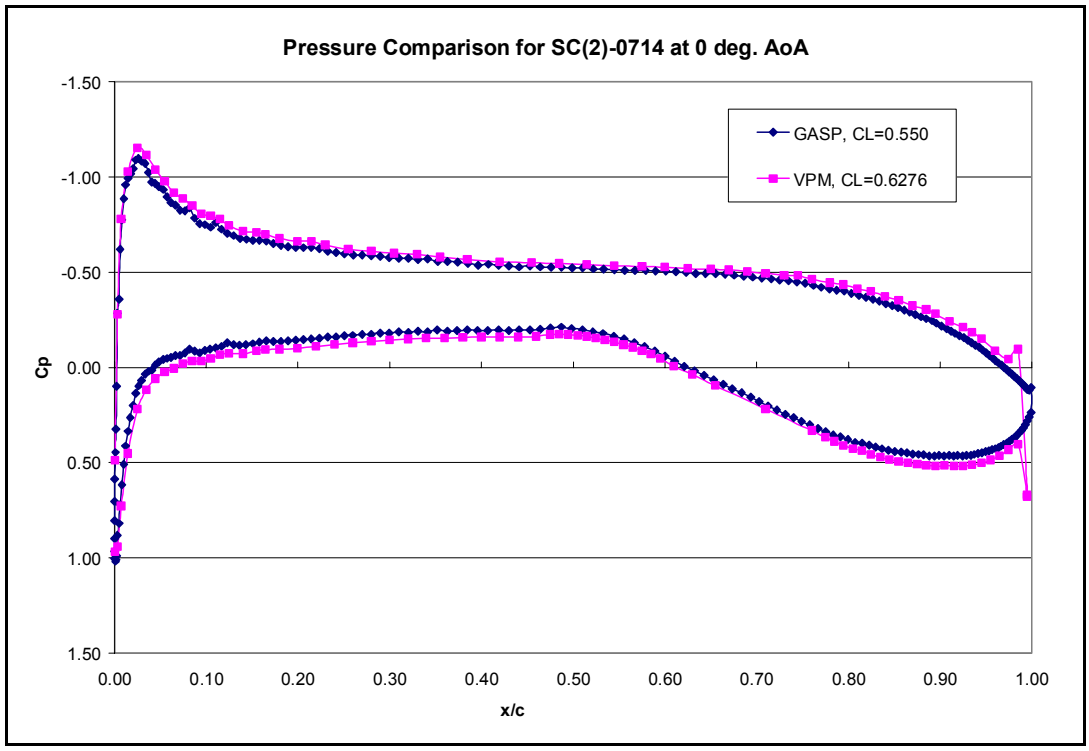

Figure 4.7: Pressure Distribution Comparison for SC(2)-0714 at 0 deg. AoA

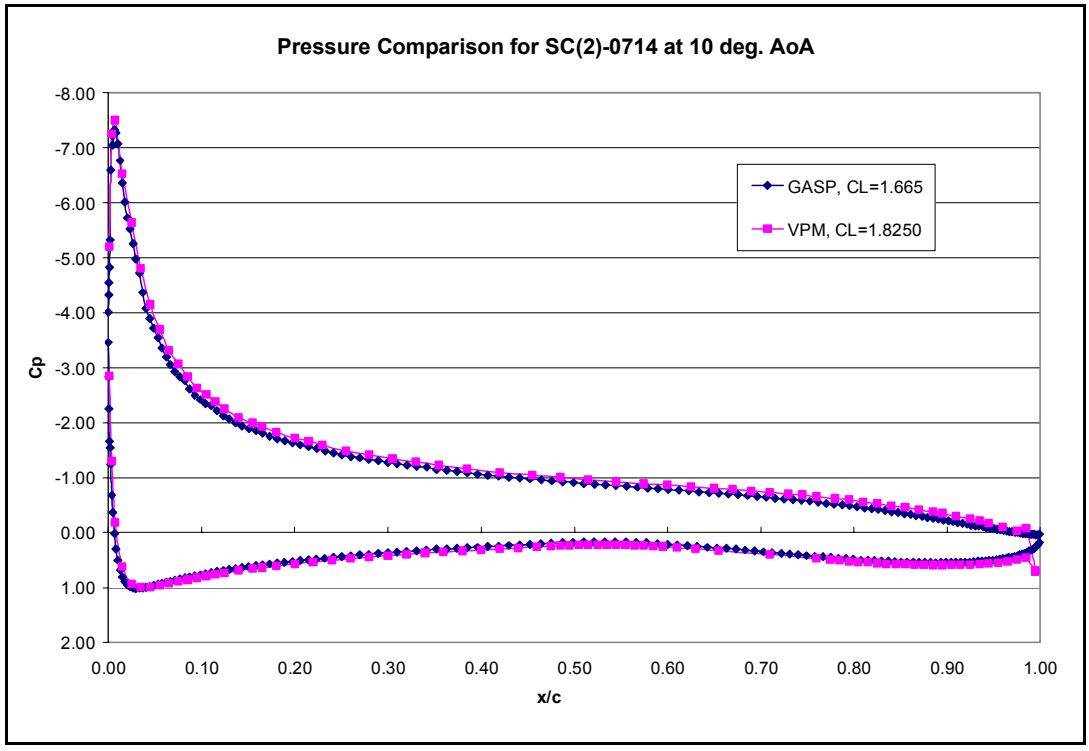

Figure 4.8: Pressure Distribution Comparison for SC(2)-0714 at 10 deg. AoA

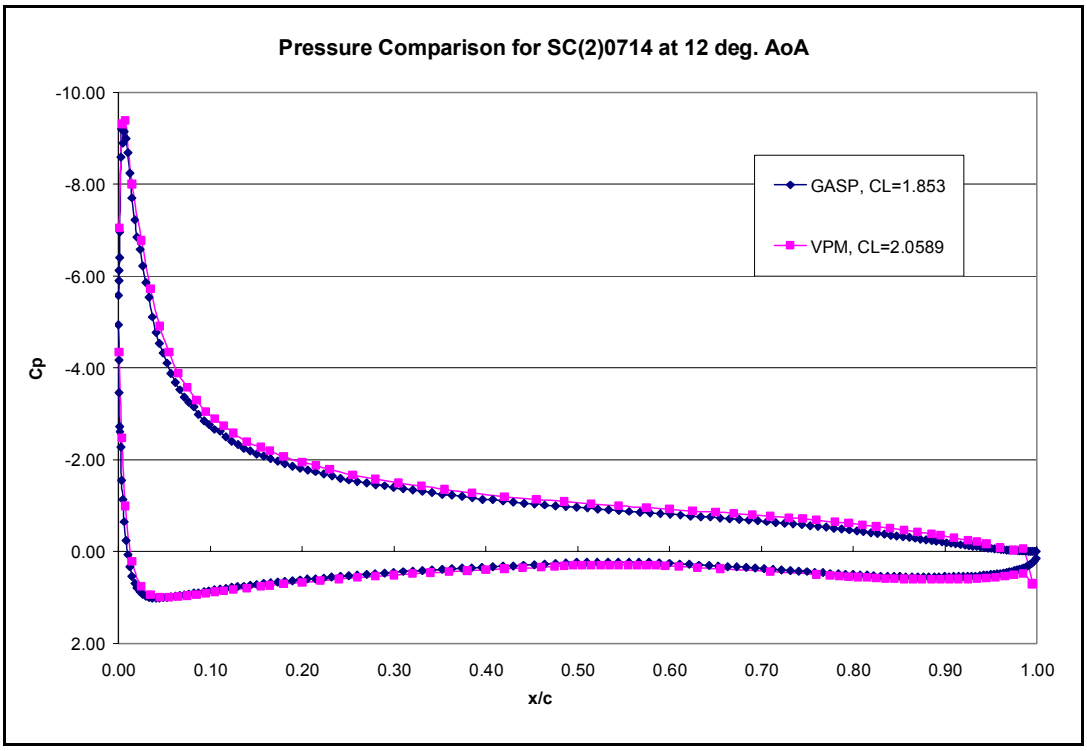

Figure 4.9: Pressure Distribution Comparison for SC(2)-0714 at 12 deg. AoA

These results show that the Boundary Layer Applets can be used to obtain fairly accurate results for low lift coefficients, but they are less accurate as C_L is increased. This method would be favorable to use as a way to predict trailing edge noise within some small amount of error because it only takes a few hours to run these applets where as it takes days to run the CFD codes. This VPM/BL approach seems to work fairly well up to modest lift coefficients.

Chapter 5: Conclusions

In this research venture there were two main objectives. The first objective dealt with continuing to study the performance of the two-dimensional jet-wing airfoils. The second objective was to create a simplified method of calculating the trailing edge noise of an airfoil. The effort of this project was aimed at validating these methods and assessing both positive and negative consequences of each.

5.1 Jet-wing Distributed Propulsion Conclusions

The concept of distributed propulsion could be applied to many current and future aircraft as a way to improve the aircraft industry. One of the most advantageous properties of the jet-wing is possibility of improved propulsive efficiency beyond the typical $\eta_P = 80\%$ of the most efficient modern turbofan-powered aircraft [26]. This thesis attempted to show the benefits of distributed propulsion and assess any negative consequences.

This project was a continuation of one initiated by Dippold [15] to study jet-wing distributed propulsion by trying to apply a jet-wing to a thick "inboard" airfoil. In this study, the EET Wing was chosen as a realistic transonic wing which could benefit from distributed propulsion. So, an inboard airfoil section was chosen, $\eta = 0.226$, for applying the jet-wing concept. The jet-wing was applied to the inboard EET airfoil resulting in a propulsive efficiency of $\eta_P = 81\%$, which is a 1% increase from the efficiency of an efficient modern turbofan-powered aircraft. This might not seem like a big increase but it must be remembered that the typical $\eta_P = 80\%$ is an upper bound for the most efficient high-bypass-ratio turbofan engines and most have an efficiency much lower than this. Also, the propulsive efficiency calculated for this project only includes the jet-wing portion of the hybrid distributed propulsion approach so the actual efficiency will be different.

Another important conclusion found through this research project is the fact that this inboard EET airfoil began with a fairly thick trailing edge. This allowed for the jet-wing to be added without doubling the trailing edge thickness as Dippold [15] had to do for his thinner "outboard" airfoils. The jet-wing increased the propulsive efficiency for this case over the nominal $\eta_P = 80\%$ that is the case for modern aircraft without any modifications and the unwanted effect of increasing drag.

5.2 Trailing Edge Noise Metric Conclusions

Decreasing the amount of noise produced during take-off, landing and cruise is one of the main goals of aircraft designers today. Trailing edge noise is one of the main contributors to airframe noise and so the decrease of this source would give designers a good start at reaching their goals. Hosder et al [20] has developed a noise metric that is a good indicator of trailing edge noise but the comprehensive CFD calculations used in their studies was very computationally expensive. Developing a method that is less computationally expensive, which is another goal of this project, would be very appealing to those attempting to calculate trailing edge noise. This thesis attempted to assess the accuracy of a simplified method compared to the full CFD runs.

The supercritical airfoil, SC(2)-0714, was used to run the Virginia Tech Boundary Layer Applets to obtain boundary layer data which was used to calculate the characteristic turbulent length scale and the characteristic turbulent velocity. Three methods were used to calculate these values as a comparison with those results obtain from GASP by Hosder [20]. Two of the methods, one using a mixing length model and another using a TKE model, set the eddy viscosity in the log region equal to the eddy viscosity in the outer region of the boundary layer. The last method used a TKE model that actually printed out the TKE values. A maximum TKE value was obtained and used to calculate the turbulent length scale and turbulent velocity. The results for these three

methods compared fairly well with the GASP results at low lift coefficients with the accuracy decreasing as C_L increased. The calculations of the characteristic turbulent velocity showed better comparison with the GASP results when the results with the max TKE value actually calculated by the applets were used. This led to the decision that this method would be good enough to be used as a final calculation of trailing edge noise for cases run up to modest lift coefficients.

References

[1] Callaghan, J. T., and Liebeck, R. H., "Some Thoughts on the Design of Subsonic Transport Aircraft for the 21st Century," SAE Paper No. 901987, October 1990.

[2] Guynn, M. D., Olson, E. D., "Evaluation of an Aircraft Concept with Over-Wing, Hydrogen-Fueled Engines for Reduced Noise and Emissions," NASA TM-2002-211926, September 2002.

[3] Spence, D. A., "The Lift Coefficient of a Thin, Jet-Flapped Wing," *Proceedings of the Royal Society of London, Series A, Mathematical and Physical Sciences*, Volume 238, Issue 112, Dec., 1956, pp 46-68.

[4] Yaros, S. F., Sextone, M. G., Huebner, L. D., Lamar, J. E., McKinley, Jr., R. E., Torres, A. O., Burley, C. L., Scott, R. C., Small, W. J., "Synergistic Airframe-Propulsion Interactions and Integrations," NASA TM-1998-207644, March 1998.

[5] Dippold, Vance, Hosder, Serhat, and Schetz, Joseph A., "Analysis of Jet-Wing Distributed Propulsion From Thick Wing Trailing Edges," 42nd Aerospace Sciences Meeting and Exhibit, AIAA 2004-1205, Reno, NV, January 5-8, 2004.

[6] Kuchemann, D., *The Aerodynamic Design of Aircraft*, Pergamon Press, New York, 1978, pp. 229.

[7] Bertin, J. J. and Smith, M. L., *Aerodynamics for Engineers*, 3rd Ed., Prentice Hall, New Jersey, 1998.

[8] Drela, M., "A User's Guide to MSES 2.95," MIT Computational Aerospace Sciences Laboratory, Sept., 1996.

[9] Drela, M., "MSES Multi-element Airfoil Design/Analysis Software – Summary," http://raphael.mit.edu/projects%26research.html, Massachusetts Institute of Technology, MA, May, 1994.

[10] Devenport, W., Kapania, R., Rojiani, K., and Sigh, K., *Java Applets For Engineers*, http://www.engapplets.vt.edu.

[11] Schetz, J. A., *Boundary Layer Analysis*,Prentice Hall, New Jersey, 1993.

[12] *GASP Version 4.1.1 Reference Guide*, Aerosoft, Inc, Blacksburg, VA.

[13] *Gridgen Version 14 User Manual*, Pointwise, 2002.

[14] Ko, Y.-Y. A, "The Multidisciplinary Design Optimization of a Distributed Propulsion Blended-Wing-Body Aircraft," Ph.D. Dissertation, Virginia Polytechnic Institute & State University, April, 2003.

[15] Dippold, Vance F., "Numerical assessment of the performance of jet-wing distributed propulsion on blended-wing-body aircraft," Master's Thesis, Virginia Polytechnic Institute & State University, August, 2003.

[16] Jacobs, Peter F., and Gloss, Blair B., "Longitudinal Aerodynamic Characteristics of a Subsonic Energy-Efficient Transport Configuration in the National Transonic Facility," NASA TP-2922, August 1989.

[17] Mason, W. H., Configuration Aerodynamics Notes, Chapter 6: Subsonic Aerodynamics of Airfoils and Wings, pp. 39-40. http://www.aoe.vt.edu/~mason/Mason_f/ConfigAeroSubFoilWing.pdf

[18] Allison, Dennis O., and Cavallo, Peter A,. "Static Aeroelastic Predictions for a Transonic Transport Model Using an Unstructured-Grid Flow Solver Coupled With a Structural Plate Technique," NASA TP-2003-212156, March 2003.

[19] *Boeing 777 Program Information*, Boeing, http://www.boeing.com/commercial/777family/flash.html

[20] Hosder, Serhat, Schetz, Joseph A., Grossman, Bernard, and Mason, William H., "Airframe Noise Modeling Appropriate For Multidisciplinary Design and Optimization," 42nd Aerospace Sciences Meeting and Exhibit, AIAA 2004-0698, Reno, NV, January 5-8, 2004.

[21] Thompson, J. F., ed., Bharat, K. S., ed., and Weatherhill, N. P., ed., *The Handbook of Grid Generation*, CRC Press, Washington, DC, 1999.

[22] *Blended Wing Body Design Group Website*, Virginia Tech, http://www.aoe.vt.edu/research/groups/bwb/

[23] *NASA Aeronautics Blueprint: Toward a Bold New Era in Aviation*, NASA, http://www.aerospace.nasa.gov/aero_blueprint/cover.html

[24] Attinello, J. S., "The Jet-wing," IAS Preprint No. 703, IAS 25th Annual meeting, Jan. 28-31, 1957.

[25] Ko, A., Schetz, J. A., Mason, W. H., "Assessment of the Potential Advantages of Distributed-Propulsion for Aircraft," XVIth International Symposium on Air Breathing Engines (ISABE), Cleveland, OH, Paper 2003-1094, Aug. 31 - Sept. 5, 2003.

[26] Hill, P. and Peterson, C., *Mechanics and Thermodynamics of Propulsion*, 2nd Ed., Addison-Wesley, New York, 1992.

[27] *Marine Engineering*, Vol. 1, Society of Naval Architects & Marine Engineers, Ed. Herbert Lee Seward, pp. 10-11.

[28] Antoine, N. E. and Kroo, I. M. "Aircraft Optimization For Minimal Environmental Impact," AIAA Paper 2002-5667, September 2002.

[29] Goldstein, M. E. *Aeroacoustics.* McGraw-Hill Book Company, New York 1976.

[30] Lilley, G. M. "The prediction of Airframe Noise and Comparison with Experiment." *Journal of Sound and Vibration,* **239**(4):849-859, 2001.

[31] Lilley, G. M. "A Study of the Silent Flight of the Owl," AIAA Paper 1998-2340, 1998.

Appendix A: Tabulated Airfoil Coordinates

A.1 EET Inboard Airfoil Coordinates

x/c	y/c (U.S)	y/c (L.S)
0.00000	0.00000	0.00000
0.00200	0.00862	-0.01115
0.00500	0.01443	-0.01622
0.01000	0.02034	-0.02158
0.02000	0.02777	-0.02826
0.03000	0.03258	-0.03281
0.04000	0.03606	-0.03639
0.05000	0.03896	-0.03938
0.06000	0.04151	-0.04201
0.07000	0.04383	-0.04446
0.08000	0.04587	-0.04678
0.09000	0.04769	-0.04895
0.10000	0.04935	-0.05094
0.11000	0.05075	-0.05279
0.12000	0.05202	-0.05452
0.13000	0.05316	-0.05612
0.14000	0.05417	-0.05762
0.15000	0.05508	-0.05902
0.16000	0.05588	-0.06032
0.17000	0.05660	-0.06155
0.18000	0.05724	-0.06267
0.19000	0.05778	-0.06372
0.20000	0.05829	-0.06470
0.22000	0.05911	-0.06643
0.24000	0.05969	-0.06780
0.26000	0.06005	-0.06894
0.28000	0.06021	-0.06982
0.30000	0.06021	-0.07041
0.32000	0.06007	-0.07076
0.34000	0.05977	-0.07087
0.36000	0.05929	-0.07075
0.38000	0.05866	-0.07041
0.42000	0.05696	-0.06919
0.46000	0.05482	-0.06727
0.50000	0.05218	-0.06456
0.52000	0.05074	-0.06289
0.54000	0.04916	-0.06095
0.56000	0.04747	-0.05883
0.58000	0.04568	-0.05643
0.60000	0.04374	-0.05388
0.62000	0.04171	-0.05111
0.64000	0.03958	-0.04818
0.66000	0.03739	-0.04507
0.68000	0.03515	-0.04184
0.70000	0.03284	-0.03844
0.72000	0.03041	-0.03498
0.74000	0.02788	-0.03148
0.76000	0.02531	-0.02797
0.78000	0.02265	-0.02455
0.80000	0.01991	-0.02128
0.82000	0.01706	-0.01827
0.84000	0.01415	-0.01560
0.86000	0.01116	-0.01335
0.88000	0.00811	-0.01169
0.90000	0.00498	-0.01068
0.92000	0.00177	-0.01042
0.94000	-0.00150	-0.01093
0.96000	-0.00486	-0.01221
0.98000	-0.00832	-0.01432
1.00000	-0.01186	-0.01727

A.2 SC(2)-0714 Coordinates

x/c	y/c
1.000000	-0.013000
0.990000	-0.010135
0.980000	-0.007570
0.970000	-0.005305
0.960000	-0.003340
0.950000	-0.001675
0.940000	-0.000310
0.930000	0.000755
0.920000	0.001520
0.910000	0.001985
0.900000	0.002250
0.890000	0.002315
0.880000	0.002080
0.870000	0.001645
0.860000	0.001010
0.850000	0.000175
0.840000	-0.000860
0.830000	-0.002095
0.820000	-0.003530
0.810000	-0.005065
0.800000	-0.006700
0.790000	-0.008535
0.780000	-0.010470
0.770000	-0.012505
0.750000	-0.016775
0.670000	-0.034655
0.640000	-0.041060
0.620000	-0.045130
0.600000	-0.049000
0.590000	-0.050835
0.580000	-0.052570
0.570000	-0.054205
0.560000	-0.055740
0.550000	-0.057175
0.540000	-0.058510
0.530000	-0.059745
0.520000	-0.060880
0.510000	-0.061915
0.500000	-0.062850
0.490000	-0.063685
0.480000	-0.064420
0.470000	-0.065055
0.450000	-0.066125
0.430000	-0.066995

x/c	y/c
0.410000	-0.067665
0.390000	-0.068135
0.370000	-0.068405
0.350000	-0.068475
0.330000	-0.068345
0.310000	-0.068015
0.290000	-0.067485
0.270000	-0.066755
0.250000	-0.065825
0.230000	-0.064695
0.210000	-0.063365
0.190000	-0.061835
0.170000	-0.060105
0.160000	-0.059140
0.150000	-0.058075
0.130000	-0.055745
0.120000	-0.054480
0.110000	-0.053015
0.100000	-0.051450
0.090000	-0.049785
0.080000	-0.048020
0.070000	-0.045955
0.060000	-0.043690
0.050000	-0.041125
0.040000	-0.038060
0.030000	-0.034395
0.020000	-0.029530
0.010000	-0.022365
0.005000	-0.016563
0.002000	-0.010763
0.000000	0.000000
0.002000	0.010763
0.005000	0.016563
0.010000	0.022365
0.020000	0.029530
0.030000	0.034495
0.040000	0.038160
0.050000	0.041225
0.060000	0.043790
0.070000	0.046055
0.080000	0.048120
0.090000	0.049885
0.100000	0.051550
0.110000	0.053115

x/c	y/c
0.120000	0.054480
0.130000	0.055745
0.150000	0.058075
0.160000	0.059140
0.170000	0.060105
0.190000	0.061835
0.210000	0.063365
0.220000	0.064030
0.240000	0.065160
0.270000	0.066555
0.290000	0.067285
0.320000	0.068080
0.340000	0.068410
0.370000	0.068605
0.400000	0.068500
0.440000	0.067960
0.470000	0.067255
0.500000	0.066250
0.530000	0.064945
0.560000	0.063340
0.590000	0.061435
0.610000	0.059965
0.640000	0.057460
0.660000	0.055590
0.680000	0.053520
0.700000	0.051250
0.720000	0.048780
0.740000	0.046110
0.750000	0.044675
0.770000	0.041605
0.790000	0.038335
0.800000	0.036600
0.820000	0.032930
0.830000	0.030995
0.850000	0.026925
0.860000	0.024790
0.880000	0.020320
0.890000	0.017985
0.900000	0.015550
0.920000	0.010480
0.930000	0.007845
0.940000	0.005110
0.950000	0.002275
0.970000	-0.003595
0.980000	-0.006630
0.990000	-0.009765
1.000000	-0.013000

Vita

Jessica Nicole Walker was born on April 23, 1980 in Cheverly, Maryland. She is the oldest child of Bryan and Julie Walker, Sr., with a younger brother, Bryan and a younger sister, Brittany. Jessica and her parents lived in Lothian, Maryland until they moved to Calvert County, Maryland when she was eight. Jessica gradated fourth in her class from Northern High School in Owings, Maryland in 1998. That fall she began her undergraduate career at Virginia Tech studying Aerospace and Ocean Engineering. In her senior year, she was a member of an international design team, where 9 aerospace and 3 ISE students from Virginia Tech teamed up with 12 aerospace engineering students from Loughborough University in Loughborough, UK. Her team took 2nd Place in the 2002 NASA SATS competition. Jessica graduated Cum Laude from Virginia Tech in 2002 with a Dual Bachelor's degree in Aerospace and Ocean Engineering. After graduating with her Bachelor's degree, Jessica decided to continue her education and stayed on at Virginia Tech to complete her graduate degree. After Jessica finishes her Master's degree in Aerospace engineering, she plans to find a job in aerodynamics in the Maryland-Virginia area.